Journal of The
Electrochemical Society

Novel Methodology of General Scaling-Approach Normalization of Impedance Parameters of Insertion Battery Electrodes – Case Study on Ni-Rich NMC Cathode: Part I. Experimental and Preliminary Analysis

To cite this article: Marko Firm *et al* 2024 *J. Electrochem. Soc.* **171** 120540

Journal of The Electrochemical Society, 2024 **171** 120540

Novel Methodology of General Scaling-Approach Normalization of Impedance Parameters of Insertion Battery Electrodes – Case Study on Ni-Rich NMC Cathode: Part I. Experimental and Preliminary Analysis

Marko Firm,[1,2] Jože Moškon,[1,z] Gregor Kapun,[1] Sara Drvarič Talian,[1] Ana Rebeka Kamšek,[1,2] Mateja Štefančič,[3] Samo Hočevar,[4] Robert Dominko,[1,2] and Miran Gaberščček[1,2,z]

[1]*Department of Materials Chemistry, National institute of Chemistry, 1000 Ljubljana, Slovenia*
[2]*Faculty of Chemistry and Chemical Technology University of Ljubljana, 1000 Ljubljana, Slovenia*
[3]*Slovenian National Building and Civil Engineering Institute, 1000 Ljubljana, Slovenia*
[4]*Department of Analytical Chemistry, National Institute of Chemistry, 1000 Ljubljana, Slovenia*

In PART-1 of this paper, we present a generally applicable experimental methodology and a preliminary analysis strategy that can help researchers in the field of batteries to perform relevant measurements and a simple initial check of the self-consistency of the obtained impedance data of lithium-ion insertion electrodes. Using a model system based on a Ni-rich NMC active material, we demonstrate the necessary experimental steps to perform reliable and accurate impedance measurements of active electrodes (cells) and the characterization techniques required for a meaningful analysis of the obtained impedance data. We demonstrate the practical application of a simple preliminary analysis in which mass normalization of impedance spectra together with the assumption of ideal capacitive behavior allows access to the total (chemical) insertion capacitance, C_{total}, of the studied active material in an electrode. Furthermore, we show for the first time that there is an exact quantitative relationship (equality) between C_{total}, and the differential capacitance, C_d, of porous insertion electrodes. A series of impedance data obtained by systematically varying the NMC cathode mass (thickness) is further analyzed step by step in PART-2. Therein, we explain in detail the approach of analyzing impedance spectra using an advanced physics-based Transmission Line Model (TLM) and demonstrate the practical applicability of the scaling methodology. The main objective of PART-1 is to provide experimenters with directly applicable tools and skills to develop a basic intuition for exploring and explaining the key phenomena observed in the impedance responses of porous Li-ion insertion cathodes. PART-2 will highlight the major advantages of analyzing impedance data using physics-based models. Any model that is based on elements with physical meaning and is correct should pass the "consistency test" included in the scaling relations.

 [DOI: 10.1149/1945-7111/ada061]

Manuscript submitted August 21, 2024; revised manuscript received October 31, 2024. Published December 30, 2024.

Supplementary material for this article is available online

Electrochemical impedance spectroscopy is considered one of the most accurate electrochemical methods. At the same time, state-of-the-art equipment and well-designed measuring cells are widely available. This has led to impedance spectroscopy being used much more frequently in many areas of electrochemistry, including battery research. However, the biggest bottleneck is still the reliable analysis of the measured spectra. To get a first idea of the possible explanation of the different impedance contributions, researchers today can use various software that can describe the measurements in terms of simple equivalent circuits of resistors, capacitors and inductors. The problem is that equivalent circuits alone cannot provide direct physical insight into the system under investigation, as a particular electrical element is not necessarily uniquely associated with a physical parameter or set of such parameters.[1]

To avoid the ambiguities associated with using simple equivalent circuits, one of the physics-based approaches to modelling impedance can be chosen. These can essentially be divided into three categories: (i) analytical[2,3] or (ii) numerical[4,5] solutions of the transport/response equations or (iii) the use of so-called transmission lines (TL) by applying the same equations.[1,6] Despite their ability to provide a direct qualitative and quantitative insight into the actual processes occurring in a given electrochemical system (batteries, etc.), physics-based approaches still seem to be less popular than the use of arbitrary equivalent circuits. One of the reasons for this appears to be that the former is much more complex to analyze, i.e. mathematically more demanding.[7–9] Moreover, precise mathematical models, e.g. those based on the Poisson-Nernst-Planck framework or Newman's porous electrode theory,[1–6] tend to contain more parameters than can be reliably extracted from a single impedance spectrum (this is known as the model overparameterisation problem).

Recently, we have published a number of papers in which the TL approach has been successfully used to describe the impedance of battery cells containing one or more porous components,[10–14] including showing that the model can successfully describe all the main features observed in impedance measurements of NMC cathodes in a wide frequency range (MHz-mHz). However, some details related to the low-frequency diffusion phenomena remained mainly qualitatively explained, e.g. the detection of individual arcs/contributions at certain conditions in the cells. The study has shown that further verification of the model is needed, especially at the lowest frequencies where the overlap of processes is most critical.

This study provides additional experiments that confirm the good predictive ability of the above-mentioned transmission line model for porous battery electrodes. Specifically, we fabricated a series of NMC cathodes with different thicknesses (masses) in a wide range from about 15 μm to about 140 μm, corresponding to an active mass loading between about 1.2 mg·cm^{-2} and about 29 mg·cm^{-2}. However, the first experiments have already shown that a lot of time has to be invested in optimizing the measurement conditions in order to quantitatively analyze a set of electrodes with large differences in thickness. This is because the experimental data may contain various systematic errors, in particular due to inappropriate set-up of the measurement cell or inappropriate protocols for the impedance measurements themselves. Here we try to minimize these errors so that satisfactory repeatability is achieved over a wide range.

[z]E-mail: joze.moskon@ki.si; miran.gaberscek@ki.si

Due to the many experimental details and the detailed description of the agreements and disagreements between model and experiments, the study is divided into two parts: (i) The first part is dedicated to the detailed description of the experiments (electrochemical, compositional, morphological), but also to the basic description of the model and the expected scaling correlations to be tested with the present experiments. In addition, a brief empirical analysis of the experiments is performed and general scaling relationships of the impedance parameters with electrode thickness/mass are presented. (ii) The second part deals with the detailed quantitative analysis of the measured impedance spectra using the developed physics-based transmission line model. All measured features from 10^6 Hz to 10^{-4} Hz are analyzed. The agreement with and deviation from the model predictions are commented in detail.

We show here that physics- based modelling can be used effectively to analyze some battery characteristics, even if one is not willing to invest the time to implement the full models. Indeed, among other things, physical models contain some general predictions about the behaviour of impedance spectra under various conditions of interest. A trivial example of this is that the trends in the high-frequency intercept of the complex in-plane impedance can reveal the trends in electrolyte conductivity. In contrast, a lesser known fact—which is also predicted by physical modelling - is that for battery electrodes, the imaginary part of the impedance (-Im(Z)) read at a sufficiently low frequency (e.g. 1 mHz) is inversely proportional to the mass of the active insertion material. We use here many other simple relationships derived from physical models to demonstrate the good agreement between the state-of-the-art models and the actual impedance measurements of insertion batteries. To keep the study coherent, we mainly focus on one aspect, namely the scalability of electrodes, i.e. the dependence of the impedance parameters on the electrode size, more precisely on its thickness (or mass per unit geometric area).

Experimental

Materials and methods.— *NMC active material.*—The Lithium Nickel Manganese Cobalt Oxide (NMC) material was provided by MSE Supplies® and was used in the form in which it was supplied (no treatment). Elemental analysis (ICP-OES) revealed the composition $LiNi_{0.83}Mn_{0.06}Co_{0.11}O_2$ (oxygen content assumed); therefore, we use the abbreviation NMC83-06-11 here. The particle size distribution of the NMC material was analyzed on the SEM image at 400x magnification. For segmentation, QuPath software was used to manually delineate 500 particles within the visible area.[15] Binary masks (black and white) were then exported from QuPath for each marked particle. A custom Python script was used to determine the areas and perimeters of the particles and derive their circularities and the diameters of the equivalent spheres (details in SI).

Electrode preparation.—NMC powder, carbon black (Super C65T, Imerys), and PolyVinylene DiFluoride (PVDF, Sigma Aldrich) in mass ratio 90:5:5 were mixed together with N-Methyl-2-Pyrrolidone (NMP, Merck) in a shaker mixer/mill (SPEX SamplePrep) for 60 min. The resulting ink (slurry) was applied to carbon-coated aluminum foil (Armor, France) using a doctor blade mounted on an automatic coating machine (MTI Corporation). The coated electrode film was first dried at 80 °C in a dynamic vacuum for at least 3 h. The final NMC coating had a mass loading ranging from 0.7 to 31 mg·cm^{-2}. The circular cathodes with a geometric area of 2 cm^2 were cut and pressed with a hydraulic hand press (Specac) with a force of 1.25 t·cm^{-2} (resulting in a porosity of about 40%). The final thickness of the cathodes ranged from about 14 μm for the thinnest to 140 μm for the thickest electrodes. In a second step, the cathodes were dried overnight under dynamic vacuum at 110 °C and transferred to to an argon-filled glove box (MBraun) with a water and oxygen content of less than 1 ppm. The anodes were prepared in a glove box from a 200 μm thick lithium metal foil (Gelon), which was cut into circles with an area of 2.5 cm^2. The lithium surface was carefully scraped and rolled to expose a fresh metal surface. For the lithium reference electrode (RE) used for the Galvanostatic Intermittent Titration Technique (GITT), the lithium metal foil was thinned on one side and cut into a triangular shape with a very narrow tip. To perform the so-called 3-electrode impedance measurements, a 4 cm long and 50 um thick Au wire with a 7 um thick insulating layer of polyimide (Goodfellow) was used. On one side, 0.3 mm of the insulation was removed by heat treatment. On the other side, the wire was spot-welded to a copper (20 μm foil) current collector.

SEM.—A field emission scanning electron microscope (FE-SEM) Apreo 2 S (Thermo Fisher Scientific, Netherlands) equipped with an Ultim Max 100 energy dispersive spectrometer (Oxford, UK) was used to analyze the NMC material and electrodes by scanning electron microscopy (SEM).

FIB-SEM.—The cross-sectional analysis was performed with the FIB−SEM (Focused Ion Beam Scanning Electron Microscope) Helios Nanolab 650 (Thermo Fisher Scientific, Netherlands) equipped with a Pt gas injection system (GIS), a vacuum transfer lock ALTO 1000 (Gatan, US) and an energy dispersive spectrometer SDD X-Max 50 (Oxford, UK). For the experimental details see SI (Fig. S4).

Electrode porosity.—The porosity of the cathodes was calculated based on the mass, thickness, composition and physical densities of the composite components. The thickness was determined using a gauge (Garant). To validate the accuracy of the porosity calculations, Mercury intrusion porosimetry (MIP) was performed on samples with different mass loadings (5 mg·cm^{-2}, 11 mg·cm^{-2}, and 22 mg·cm^{-2}). The measurements were carried out with the AutoPore IV 9500 porosimeter (Micromeritics). The sample weight was typically 0.36 g. The porosimeter operated in a pressure range of 0.004–413 MPa, corresponding to a pore size of 403 μm to 0.0037 μm, based on the Washburn model.[11] The measurements were carried out in two stages: first in the low-pressure regime (0.004–0.345 MPa) and then in the high-pressure regime (0.1–413 MPa). Since the D90 value (SEM) is (21.8 ± 0.7) μm, only diameters of less than 22 um were considered as cathode porosity. The pore/void volume filled at lower pressures (larger diameter) corresponds to the penetration of Mercury into the space between the electrodes in a measured sample.[16]

Cell assembly.—The pouch cells were assembled in glove box filled with Ar by properly stacking the electrodes and separator and sealing them in a Triplex foil with pre-prepared 3 mm wide foil strips for the contacts (Al for the cathode, Cu for the anode and RE in 3-electrode cells). The separator used was glass microfiber filter paper GF/A (Whatman) with a thickness of 260 μm (manufacturer specification) which was compressed to the final thickness of about 208 μm during assembly into the pouch cell (the calculated porosity was 88%). The geometric surface area of the separator was 3.14 cm^2. Commercially prepared 1 M $LiPF_6$ in EC/DEC = 1:1 vol (LP40, E-lyte) solution was used as electrolyte. In 3-electrode cells with gold microwire RE, 1 M $LiPF_6$ in EC/EMC = 3:7 vol (LP57, E-lyte) solution was used. The electrolyte was distributed as follows: 1 μl per mg of active material for the cathode (or minimum 10 μl), 15 μl for the Li anode and 70 μl for the separator. In the 3-electrode NMC‖RE(Au)‖CE(Li) cell, 270 μl of electrolyte was added for 2 separators. Symmetric NMC-NMC and Li-Li cells were assembled from two starting (pre-cycled) Li-NMC cells with matching NMC mass loading. For the preparation of the NMC-NMC cells, a fresh separator and a fresh electrolyte were used, while the original separator remained attached to the Li anodes and 100 μl (50 μl per separator) of additional (fresh) electrolyte was added, followed by sealing in a pouch-bag cell.

Electrochemical measurements.—NMC-Li cells were first pre-cycled to complete the initial "formation" processes (e.g. the observed initial "activation" of the NMC material). Cells were cycled for 3 cycles in CC-CV charge and CC discharge mode between 2.8 V and 4.3 V (vs Li). The first cycle was performed with a current density of C/15, followed by 2 cycles of C/10 and a 3-hour open-circuit relaxation. After relaxation, the cells were discharged to 2.8 V with C/20 to achieve a reproducible lithiated state, and finally a sequence of C/20 charging steps up to 3.665 V, 3.805 V and 4.055 V was carried out. At each step, we performed a 6-hour voltage hold, followed by a potential-controlled impedance measurement (PEIS) with a perturbation with a peak amplitude of 5 mV (3.5 mV rms) in the frequency range from 1 MHz down to 0.1 mHz. To produce the symmetric NMC-NMC cells, the NMC-Li starting cells were pre-cycled in the same way as described above. The difference was that the NMC-Li cells were only charged up to a certain voltage at which we removed the cathodes (after a 6-hour voltage hold) to produce the corresponding NMC-NMC cells. Galvanostatic curves and impedance spectra of the cell were measured at room temperature (24 °C) using a VMP3 potentiostat/galvanostat (BioLogic) with a built-in impedance module.

For the GITT on the 3-electrode NMC||RE(Li)||CE(Li) cell, we performed 6 initial C/10 pre-cycles with CC-CV charging and CC discharging between 2.8 V and 4.3 V (vs Li RE) to complete the "formation" processes and thus stabilize the cell response. We then charged the cell to 4.3 V with C/20 and performed a GITT sequence with C/20 discharge pulses, followed by an appropriate relaxation periods. The first 3 pulses corresponded to 2% of the theoretical capacity, Q_{th}, followed by corresponding relaxation times of 6 h. The next 2 pulses corresponded to 3% of Q_{th} with 4 h relaxation. The next nine pulses corresponded to 5% of Q_{th} and the relaxation periods lasted 4 h. As we approached lower states of charge (open circuit voltage, OCV, below 3.67 V), we again reduced the duration of the discharge steps to increase the number of measured states in this range and gradually increased the duration of the relaxation periods to really approach the true equilibrium state. Specifically, we used 3 pulses corresponding to 3% of Q_{th} with relaxation times of 6 h, 8 h and 12 h. Then we applied 6 pulses corresponding to 1.5% of Q_{th} with relaxation times of 12 h, 2 pulses with a relaxation time of 16 h and finally 3 pulses with a relaxation time of 20 h. The last 3 pulses in the lithiation direction were performed with less than 1.5% Q_{th} (stopped by the lower cut-off voltage of 2.8 V) and with a corresponding relaxation time of 24 h. After the last relaxation, we discharged the cell with C/100 to 2.8 V and started the GITT charging sequence. The first 4 pulses corresponded to 1.5% of Q_{th}, with the relaxation time gradually decreasing in this order: 20 h, 16 h, 14 h and 12 h. The next 3 pulses corresponded to 3% of Q_{th} with a relaxation time of 12 h, 10 h and 8 h. This was followed by 2 pulses corresponding to 3% of the Q_{th} with a relaxation time of 6 h. All subsequent charging pulses up to the upper cut-off voltage of 4.3 V corresponded to 5% of the Q_{th} and had a relaxation time of 4 h. The GITT measurements were performed in chamber with controlled temperature (24 °C) using the SP-200 potentiostat/galvanostat (BioLogic).

Results

Characterization of active material (AM) and electrodes.—For the present study, a commercial Ni-rich NMC cathode material (NMC83–06–11) was used, which appears as nearly spherical secondary particles that are aggregates of packed primary particles (Fig. 1a). Figure 1b shows a close-up SEM image of the secondary particles with a rough surface reflecting the packing of the primary particles. The SEM images were primarily analyzed to obtain information on the size and shape of the AM aggregates and their main morphological features. Figure 1c shows an SEM image of a representative population of NMC aggregates with red particle outlines as a segmentation result. Further images showing the particle morphology can be seen in Figs. S1, while S2 contains examples of particle segmentation masks. The respective roundness and diameter of the equivalent spheres were determined from Fig. 1c. The results are presented in Fig. 1d, which shows a scatter plot where each data point in the circularity-diameter space represents a particle, and both variables are summarized as histograms. The size distribution is rather broad, with the most common value being around 5 micrometers but particles up to 30 micrometers in diameter also occur. The vast majority of particles are approximately spherical in shape, with the most common circularity value being around 0.85 (a perfect sphere would give a value of 1). Larger particles are generally closer to a spherical shape, while smaller particles have a wider range of circularity values. The number-based distributions of all quantities can be seen in Fig. S3.

The results of the particle size determination are also shown as a volume distribution in Fig. S3e. Although larger particles are less common, they contribute significantly to the total volume, with the extreme case of a particle at the upper end of the specified diameter, which alone makes a contribution comparable to dozens of smaller particles. The median value was calculated as $D50 = (12.9 \pm 0.1)\,\mu m$ and is shown in Fig. S3e with a red dashed line.

The thicknesses of the electrodes (L_e) were measured using a simple gauge thickness method and used to calculate the total porosity (ε_ρ) by taking into account the physical densities of the solid compounds of the coated electrode composite.[17] The unpressed cathodes exhibited a porosity of about 55%–60%, with electrode cracks contributing significantly to ε_ρ; after pressing (1 min at 1.25 tonnes per cm^2), the porosity decreased to about 40%–44% (depending on the NMC mass loading, Table I). The stated total porosity was determined as an average over 12 electrodes. To verify the correctness and accuracy of the results, an 11 $mg{\cdot}cm^{-2}$ cathode, processed identically to the ones with 40% porosity, was also analyzed using a combination of focused ion beam milling sample preparation and electron microscopy (FIB-SEM) and porosimetry.

A FIB-SEM analysis was performed on a typical NMC cathode with an NMC active mass loading of 11 $mg{\cdot}cm^{-2}$ and pressed with a force of 1.25 tonnes per 1 cm^2 (hydraulic press). The cathode was cut with a Ga ion source in a FIB chamber to create a cross-section (Fig. 2), showing the cross-section of the NMC aggregates and revealing the porous structure of the electrode composite. We found an average thickness of 49 μm, which is in good agreement with the gauge laboratory measurements (average 52 μm). SEM examination shows that the pressing (compaction) of the cathode to 40% porosity led to cracking/deformation of several NMC secondary particles and strong disintegration of some smaller aggregates (Fig. 2a), similar to the reported effects of roll-press calendering.[17] During pressing the AM particles were slightly "imprinted" in the metal Al foil, which improves adhesion and reduces the electronic contact resistance between the composite electrode and the current collector.[18–21] The EDX mapping (Fig. 2b) shows a spatial chemical uniformity of the aggregates with a uniform distribution of Ni, Mn, Co, O (Fig. S4) and shows a variable compactness of the carbon and binder domain (CBD).

In Fig. 2, we see that CBD does not fill the entire volume between the NMC particles and there are regions with larger macropores with typical dimensions in the range of 0.5 to 3 μm with the largest pores being found around part of the surface of the AM particles that were not embedded in CBD. Thus, the local inhomogeneity in the CBD distribution leads directly to the formation of larger macropores. Smaller macropores with typical sizes of about 100 to 500 nm are observed in the areas where the CBD was not uniformly compacted (Fig. S5a). In addition, a small amount of closed pores can be observed within the NMC aggregates (Fig. S5b).

Mercury intrusion porosimetry (MIP) was used to determine the porosity of the typical NMC electrode composites used in this study (Fig. 3). Pressed and unpressed cathodes with a mass loading of 22 $mg{\cdot}cm^{-2}$ were analyzed and compared to pressed cathodes with

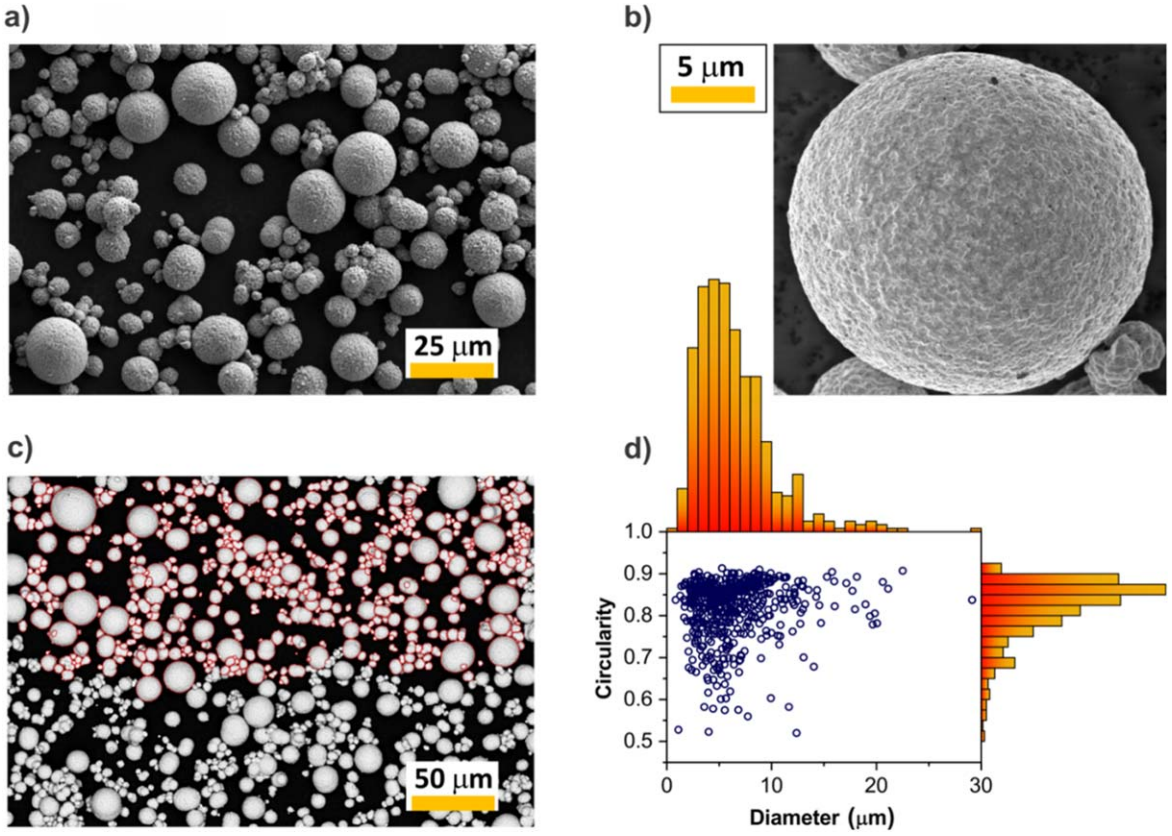

Figure 1. (a) A typical SEM image of NMC aggregates used in the present study, and (b) an SEM image of a large spherical NMC aggregate showing rough surface morphology. (c) A representative region used to determine the NMC particle (aggregate) size distribution; red particle outlines represent the segmentation results. (d) The scatter plot obtained and the corresponding histograms showing the number distributions for the equivalent sphere diameters and circularities of the NMC aggregates.

Table I. Comparison of the results of the porosity determination of the NMC cathodes by calculation based on gravimetric densities of phases (ε_ρ), and by MIP porosimetry (ε_{Hg}).

Sample	NMC mass loading [mg·cm^{-2}]	Pressing [t·cm^{-2}]	Thickness L_e [μm]	Calculated porosity ε_ρ [%]	MIP porosity ε_{Hg} [%]	Comment
A	22	0	140	60	49	Cracks contribute to ε_ρ
B	22	1.25	100	40	38	Good matching
C	11	1.25	52	44	43	Good matching
D	5	1.25	23	56	47	Non-uniform pressing

two lower loadings (11 and 5 mg·cm^{-2}); all cathodes were pressed with a force of 1.25 tonnes per 1 cm^2. In order to perform reliable and accurate porosity measurements, the mass of the sample in all cases was about 360 mg (including the mass of the Al current collectors), which corresponds to a typical mass of 300, 250, and 150 mg of the electrode composite for the respective cathodes with 22, 11 and 5 mg·cm^{-2} NMC loading. Accordingly, 10, 20, and 40 electrodes were typically placed simultaneously in the dilatometer for the measurements when the 22, 11 and 5 mg·cm^{-2} loading cathodes were analyzed. The intruded/extruded specific Hg volume, ν_{Hg}, during the pressure increase/decrease was measured in the low pressure range (0.004–0.4 MPa) and in the high pressure range (0.4–400 MPa). The *D90* value of the AM secondary particles, (21.8 ± 0.7) μm, determined by analyzing the SEM image (Fig. 1), was used as a measure of the upper limit of the pore size (diameter).[16,17] Accordingly, the analysis of the Mercury intrusion data was limited to the high pressure range. In the literature, large voids (in our case 22–403 μm) are generally attributed to the space between the samples (electrodes) in the dilatometer.[16] The pore volume due to the actual porosity of the NMC cathodes (in the considered pore diameter range from 22 μm down to 3.6 nm) was determined to be 0.11 cm^3·g^{-1} and 0.18 cm^3·g^{-1} for the 22 mg·cm^{-2} pressed and unpressed cathodes, respectively. This corresponds to a MIP porosity (ε_{Hg}) of 38% and 49%, respectively, and is in reasonable agreement with the calculated values based on the simple thickness gauge method (ε_ρ), see Table I. The obtained pore size distribution is shown in Fig. 3, where a clear bimodal distribution can be observed for both pressed and unpressed cathodes.

In the case of unpressed cathodes, the main contributions are at pore sizes of about 2.5 μm and 250 nm. For the pressed cathode with a loading of 22 mg·cm^{-2}, the first peak corresponding to the large pores between the AM particles shifts to a lower pore size of about 1.3 μm, similar as found in other studies.[17] The position of the second peak, which is generally attributed to the pores within or between the CBD clusters,[22] also shifts to a slightly lower value of about 180 nm after pressing the cathode. In the two cases of thinner cathodes, the position of the peaks is similar, although the first peak for the 11 mg·cm^{-2} cathode is at a slightly higher value

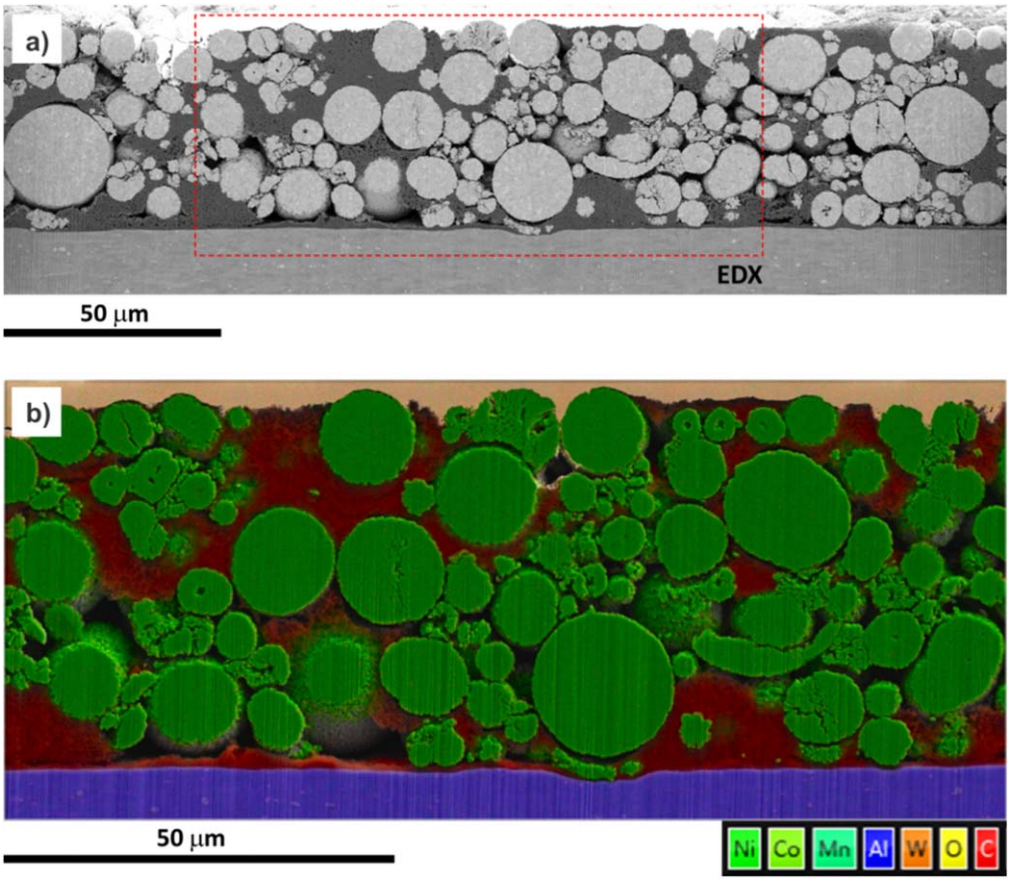

Figure 2. FIB prepared cross-section of a typical NMC cathode used in the present study with the composition NMC:CB:PVdF = 90:5:5 (wt%) and a NMC loading of 11 mg·cm^{-2} on a C-coated aluminum current collector (a) SEM shows regions with larger macropores and some partially cracked NMC aggregates; (b) EDX mapping shows the spatial chemical uniformity of the aggregates.

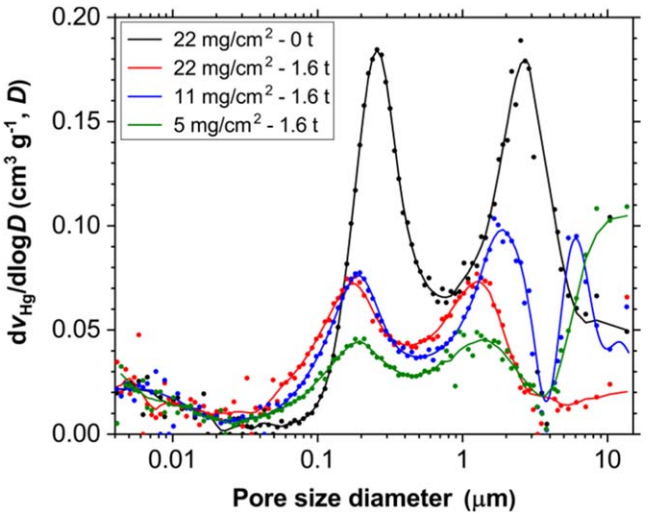

Figure 3. Results of Mercury intrusion porosimetry measurements on different NMC cathode composites, presented as differential specific pore volume with respect to the logarithm of the pore diameter ($dv_{Hg}/dlogD$), plotted as a function of the pore diameter (D).

(about 2 μm). Note that for the 11 mg·cm^{-2} cathode and especially for the 5 mg·cm^{-2} cathode, we observe a large intruded volume in the region above about 5 μm. As can be clearly seen in the FIB-prepared cross-section (Fig. 2), the surface of the cathodes exhibits considerable roughness. For the MIP measurements on thin cathodes, we used a correspondingly larger number of electrodes (see above), so that the cumulative volume between the electrodes increased proportionally. For all pressed cathodes (Fig. 3), an increase in pore volume can be observed for pores smaller than 100 nm. These pores are partly due to the compression of larger pores and partly due to the formation of additional smaller pores as a result of the cracking of NMC aggregates.[17,23]

Figure 3 shows that there is a certain population of pores in the range below 20 nm where no clear effect of pressing can be observed. One possibility is that these micropores are due to the open porosity within the NMC aggregates. A possible contribution of these micropores to the overall impedance response of the investigated cathodes is discussed in **PART-2**. As can be as seen in Table I, for samples B and C there is overall good agreement between the calculation results based on the gravimetric densities of phases ($\boldsymbol{\varepsilon_\rho}$) and the MIP porosimetry results ($\boldsymbol{\varepsilon_{Hg}}$). As expected, we find $\boldsymbol{\varepsilon_\rho > \varepsilon_{Hg}}$ for sample A (unpressed cathodes) as unpressed cathodes show some (larger) cracks that were excluded in the MIP determination. Similarly, sample D also shows $\boldsymbol{\varepsilon_\rho > \varepsilon_{Hg}}$ which can be explained by the fact that the presence of large NMC aggregates leads to non-uniform pressing of cathodes with low-loadings (thin composites).

Impedance measurement methodology.—It is generally known that insertion battery materials exhibit a specific dependence of the impedance response on the insertion lithiation level (x)[a]. In the case of lithium insertion in NMC cathodes, the dependence shows a significant variation of the surface charge transfer/incorporation resistance (R_{CT})[12,24–27] as well as changes in the medium and low

[a]Throughout the text we use label x that should in fact be considered as the average Li concentration in the formula unit of the host structure at equilibrium conditions: $x = \bar{x}$.

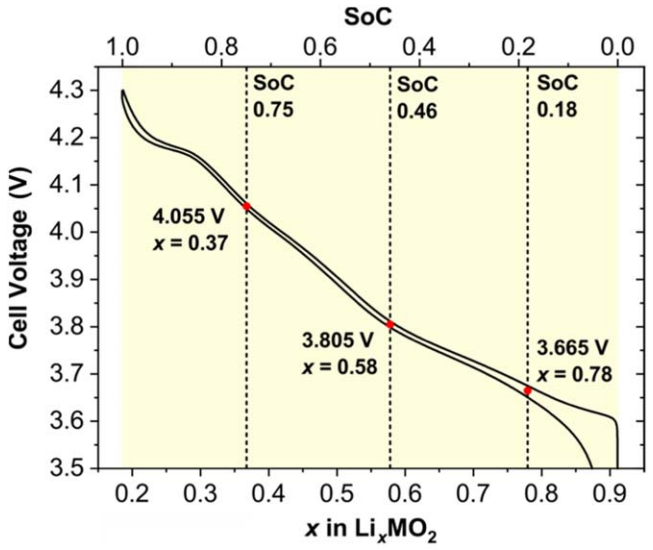

Figure 4. Selected lithiation levels (x) and the corresponding voltages at which the EIS spectra of cells based on NMC83–06–11 were measured in the present study. For comparison, the relationship between lithiation level (x) and SoC for a C/10 cycle is also depicted.

frequency range.[12,27] To cover the lithiation range accessible at both low and high current densities, we selected three lithiation levels (x) in the central region of the operating window of Ni-rich NMC materials (Fig. 4). Namely, firstly in the lower half of the SoC window ($x_1 = 0.78$, $V_1 = 3.665$ V, corresponding to typical SoC = 0.18), secondly in the middle part ($x_2 = 0.58$, $V_2 = 3.805$ V, corresponding to typical SoC = 0.46), and in the upper half of the SoC window ($x_3 = 0.37$, $V_3 = 4.055$ V, corresponding to typical SoC = 0.75).

It is important to emphasize here that the SoC parameter is not accurate enough to correctly describe the internal state of the investigated insertion electrode. In general, the internal state of a Li-ion insertion electrode is defined by the temperature (T), the pressure (p), the interfacial free energies, the coherency strain (ε), and the lithiation level (x). For compounds forming a solid solution with Li, the contribution of internal strain and changes in interfacial free energies should be zero at equilibrium, and the measured voltage polarization during the finite-rate galvanostatic cycle has a kinetic origin. Accordingly, the voltage curves in the asymptotic limit of extremely slow rates should converge towards the true thermodynamic equilibrium curve.[28] Ni-rich NMC cathode materials are assumed to have a solid solution nature—i.e. at low cycling rates, they behave as a single-phase material[29] in most of the compositional range, while the small voltage plateau between about 4.15 and 4.2 V vs $Li^+/Li°$ is due to the coexistence of two phases (H2 and H3) with limited lithium solubility.[30] On the other hand, it has been suggested that a kinetic two-phase coexistence is formed at high lithiation degrees during charging.[31]

In the present work, we have preferentially focused on the central region of the composition of the NMC material (Fig. 4, with the 3 selected x), which is determined by a single-phase mechanism. Therefore, in the selected region at constant external conditions (T, p), the internal state of the corresponding electrode, reflected in the true equilibrium potential (E_{eq} vs $Li^+/Li°$), should be defined exclusively by x. The experimentally measured open circuit voltage, V_{OC}, obtained after a sufficiently long relaxation time is therefore very close to the true equilibrium potential and should be a unique function of the state (defined by x). Similarly, a "near-equilibrium state" can be achieved at selected lithiation level (x) by performing a sufficiently long voltage hold (V_{hold}) at the same voltage value as in the open-circuit condition ($V_{hold} = V_{OC}$). A typical example of open-circuit relaxation and relaxation during voltage hold of the NMC83–06–11 cathodes is shown in Fig. 5a, where the relaxations after a previous galvanostatic +C/20 charging step are shown, with the final V_{OC} of the first cell relaxing close to $V_{hold} = V_1 = 3.665$ V of the second cell. It can be seen from Fig. 5a that, for example, one hour of relaxation is not sufficient to properly equilibrate a Ni-rich NMC cathode. Figure 5a also shows a detail when comparing the relaxation under V_{OC} and V_{hold} conditions. It appears that the NMC cathode relaxes faster under V-hold conditions than under V_{OC}. The reason for this difference is not yet known.[b] The required relaxation time under open-circuit and voltage-hold conditions is specific for each active material and different for different x.

In the present study, the selected V_1, V_2 and V_3 were subjected to a V-hold condition for 6 h prior to the impedance measurements. The duration of the voltage hold was selected based on the relaxation criterion, as described in continuation. We observed that the magnitude of the final current at the end of the 6-h voltage hold for the three selected voltages ($V_1 = 3.665$ V, $V_2 = 3.805$ V, and $V_3 = 4.055$ V) scaled approximately with the mass loading of the AM in the cathodes of the NMC-Li half-cells (Fig. 5b), with slightly larger currents observed in the case of V_3. In the latter case, these currents correspond approximately to C/2000 for small masses and are roughly in the range between C/4000 and C/5000 for other mass loadings (Fig. S6). In the case of V_1 and V_2, the final currents are about C/5000 or less for small masses and about C/4000 for medium and large mass loadings (Fig. S6). We can compare the current magnitude at the end of the voltage hold, $|I_{DC}|$(V− hold)$_{final}$, with the current magnitude during the impedance measurement, $|I_{AC}|$ (EIS,0.1mHz), of the corresponding NMC-Li half-cell at the lowest frequency of 0.1 mHz, and define the ratio k_{relax}:

$$\text{DC/AC current ratio } k_{relax}(0.1\text{mHz}) = \frac{|I_{DC}|\ (\text{V}-\text{hold})_{final}}{|I_{AC}|\ (\text{EIS})_{0.1\ \text{mHz}}} = (1-2)\ \% \quad [1]$$

The magnitude of the AC current during the impedance measurement at 0.1 mHz was determined from the corresponding amplitudes of the input voltage perturbation, $|V_{AC}|$ and the amplitude of the impedance response, $|Z|$, at 0.1 mHz: $|I_{AC}| = |V_{AC}|/|Z|$. The ratio, k_{relax}, compares the DC drift current of the system at the end of the relaxation period with the subsequent AC response due to the superimposed controlled input (voltage) perturbation. The "reference frequency" is simply the lowest frequency used for the particular impedance measurement. This is because we want to compare how large the DC drift current is compared to the impedance output signal current. The lower the minimum frequency we use, the greater the corresponding $|Z|$ and, correspondingly smaller is $|I_{AC}|$ for a certain fixed value of $|V_{AC}|$, and consequently k_{relax} increases. Thus k_{relax} corresponds to the maximum drift error of the measured impedance spectrum, which is due to the measurement at the specified minimum frequency. The obtained k_{relax} ratio is less than 1% at 3.665 V, about 1% at 3.805 V and about 2% at 4.055 V, as shown in Fig. S7 for the case of a typical NMC-Li cell. The relaxation criterion provides a direct estimate of the measurement error in the impedance measurements, where the value of the ratio k_{relax} is equal to the relative error. Accordingly, at $V_2 = 3.805$ V, for example, the expected relative measurement error of the EIS data obtained is greatest at 0.1 mHz with a value of around 1% and falls to around 0.2% at 1 mHz (Fig. S7d). Thus k_{relax} at 1 mHz drops to the level of a typical instrumental error in impedance measurements.

[b]The results such as shown in Fig. 5a suggest that "forced" relaxation during voltage-hold condition might somewhat speed up achieving equilibrium condition in electrode compared to open-circuit condition. One could speculate that additional energy (work) delivered during a voltage-hold step might help in achieving uniform (equilibrium) Li composition within the AM particles in shorter period of time. But currently there is no experimental evidence to support this interpretation (speculation).

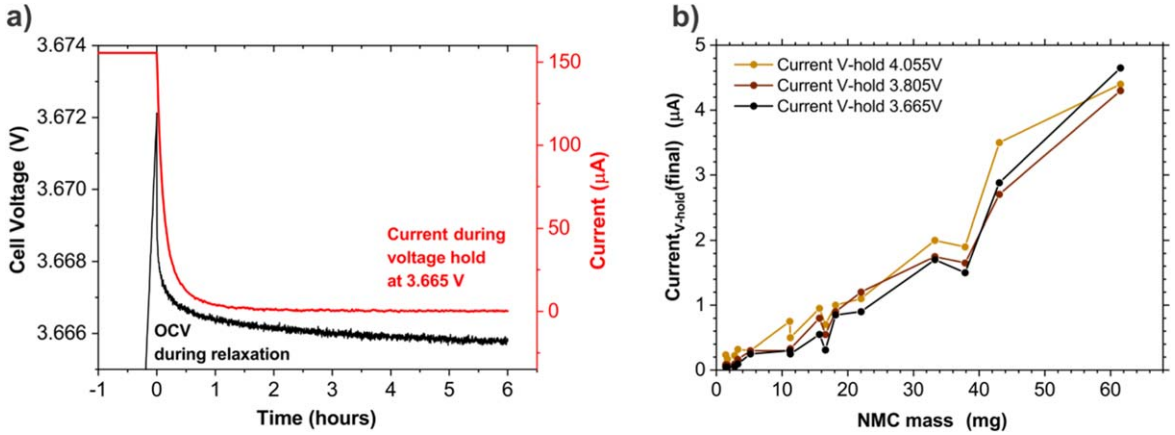

Figure 5. (a) Typical example of open-circuit relaxation and relaxation during voltage hold of the NMC83-06-11 cathodes (in the example shown, the mass of the NMC was 11.3 mg, mass loading 5.6 mg·cm^{-2}). (b) Magnitude of the final current at the end of the 6-hour voltage hold at the three selected voltages (V_1 = 3.665 V, V_2 = 3.805 V, and V_3 = 4.055 V) for different mass loadings of the cathodes in NMC-Li half cells.

Example of a typical EIS spectra of NMC-Li cells and measurement repeatability.—After initial pre-cycling and voltage hold at a selected voltage (see Experimental), the impedance responses of the NMC-Li cells were measured in the frequency range from 1 MHz down to 0.1 mHz. The EIS spectra of the individual cells were measured at three selected voltages (V_1 = 3.665 V, V_2 = 3.805 V, and V_3 = 4.055 V) under equilibrium conditions. Examples of typical EIS spectra of NMC-Li cells based on the NMC83–06–11 cathodes can be found in Fig. 6, where the EIS spectra of four NMC-Li cells with comparable masses of NMC in the cathodes (32.3, 33.2, 33.0, and 33.3 mg) and a geometric surface area of 2 cm^2 are shown in the Nyquist plot. The corresponding mass normalized spectra are shown in Fig. S8b. We note that a slight variation of the NMC cathode loading (+/− 1%) is not reflected in a variation of the corresponding EIS spectra. In fact, the imaginary component (Im(Z)) shows rather small random variations, while Re(Z) displays a larger variance between cells. As will be shown and discussed below, this pronounced variation in the EIS spectra of the NMC-Li cells is due to the variance in the impedance response of the Li metal anodes.

In Fig. S8b we see that the mass normalization of the spectra does not change the general shape of the measured impedance responses; however, it leads to tiny relative changes in the impedance magnitudes. Mass normalization of the EIS spectra therefore preserves the original information contained in the raw data. For the particular comparison case in Fig. 6 (repeatability), where the NMC mass loadings in the cathodes match quite well (repeatability of the electrode preparation on a laboratory scale), mass normalization does not provide any new information. On the other hand, mass-normalization is a very useful tool when comparing the EIS response of electrodes with different masses (see next section).

Importantly, as expected, the spectra in Fig. 6 show a specific dependence of the EIS on voltage (x).[12,24–27] We observe these differences throughout the measured frequency range, suggesting that the EIS spectra contain important information even at low frequencies well below 1 mHz. At this point, we refrain from analyzing the EIS data in detail and highlight only the most prominent features.

Figure 6b shows that there is a diffusional type of EIS response in the medium and low frequency range with a kind of impedance "hump" in the range from about 0.1 Hz down to 1 mHz, followed by a somewhat sloping impedance line at low frequencies (from around 1 mHz down to 0.1 mHz). In addition, there are consistent differences in the magnitudes of the impedance, with Re(Z) being

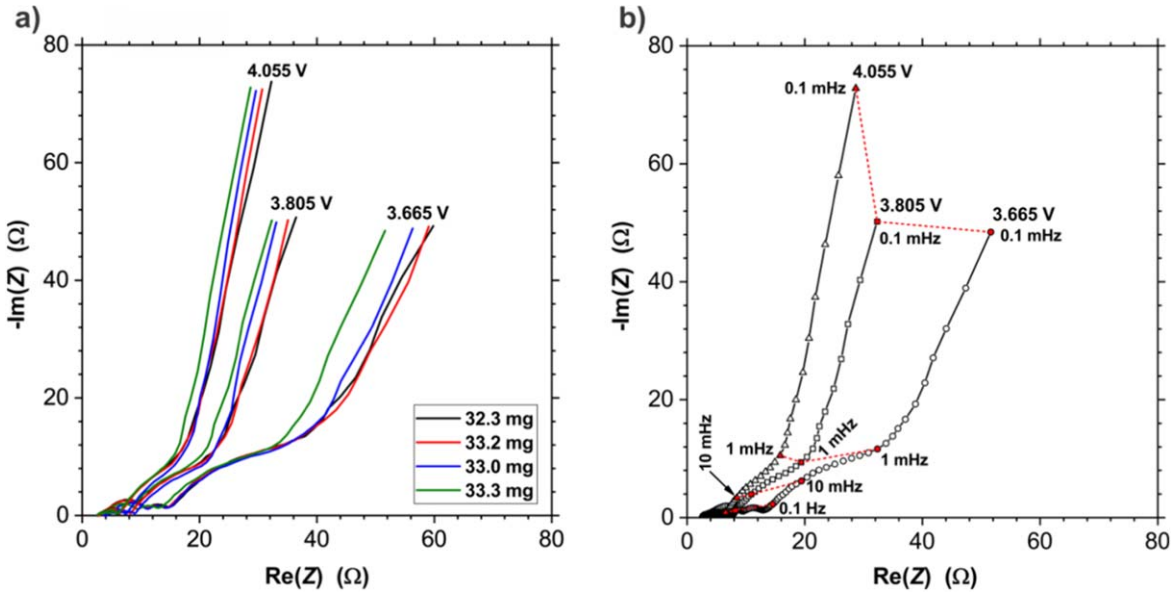

Figure 6. (a) Repeatability of the impedance spectra of NMC-Li cells with cathodes with an NMC mass loading of about 16.5 mg·cm^{-2} measured at the three selected voltages (V_1, V_2, V_3). (b) Set of typical impedance spectra of the NMC-Li cells with the characteristic frequencies shown.

largest at 3.665 V (V_1), significantly smaller at 3.805 V (V_2) and even smaller at 4.055 V (V_3). At the same time, the magnitude of Im (Z) of the impedance tail is very close to each other at V_1 and V_2, while it is significantly larger at V_3. The slope of the impedance line at low frequencies increases from $V_1 > V_2 > V_3$. The physical significance of these differences is discussed and explained in the following sections. The relatively poor repeatability of Re(Z) in the EIS responses of the NMC-Li cells (Fig. 6) cannot be correlated with the corresponding C-rate performance (SI, Fig. S9). This is also expected as the impedance of the Li metal anode varies during cycling and is strongly dependent on the current density due to current-dependent electrodeposition behavior of Li.[32,33]

Mass-normalization of EIS spectra.—In the following, we present the results of the measured impedance spectra of NMC-Li cells as a function of the electrode mass. It is shown that for thick cathodes, the real component, Re(Z), of the spectra of pre-cycled NMC-Li half cells is dominated by the contribution of the (cycled) Li anode. On the other hand, the predominant contribution to the imaginary component, Im(Z), of the low frequency part of the spectra ("impedance tail") is due to the capacitive charge storage of the cathode. Accordingly, a reasonable choice for representing such a mass dependence is to present the so-called mass-normalized spectra—instead of the surface area-normalized, as used in the conventional electrochemical studies of processes taking place at flat/planar electrodes. Indeed, in insertion batteries, the electrochemical storage properties depend on the amount (mass, volume) of active particles, so that all important impedance parameters related to charge storage (charge transfer resistance, double layer capacitance, impedance due to ambipolar diffusion within the active particles, etc) are either proportional or inversely proportional to the mass (or volume) of the active particles, as discussed in detail in the last part of this article.

In the Nyquist representation, the mass normalization of the impedance data is done simply by multiplying the magnitude of the real and imaginary components by the mass of the active material: $\mathrm{Re}(Z)_m = \mathrm{Re}(Z)\cdot m$, and $\mathrm{Im}(Z)_m = \mathrm{Im}(Z)\cdot m$. This multiplication can be seen as a generalization of the concept of mass-normalized resistance, which was introduced earlier.[34,35] The scaling procedure of mass normalization for impedance data was originally proposed by Aurbach et al.[36,37] Such normalization is particularly convenient when the focus of the analysis is at (very) low frequencies (close to or below 1 mHz), where the main storage parameters (chemical capacitance, solid-state diffusion coefficient of Li) are the main impedance contributions.[38] Despite the undisputed advantages of mass normalization in the rapid analysis of the scaling properties of storage parameters of an insertion electrode, it must be stressed that the same normalization is less suitable for transport processes that occur in the direction perpendicular to the surface of the electrode AM particles (e.g. transport in the bulk electrolyte, transport in electrode pores filled with electrolyte, etc) or occur in series with the storage (contact impedance etc.) Therefore, a graphical approach is required that separates the storage processes from the other processes that occur in series with the former, as explained in the following section.

Measured set of EIS spectra of NMC-Li cells with cathodes with different mass loadings.—Following the same procedure as described in section "Example of a typical EIS spectra of NMC-Li cells and measurement repeatability", we measured three sets of EIS spectra (at V_1, V_2 and V_3) for a series of 14 NMC-Li cells with different NMC mass loadings in the cathodes ranging from about 0.7 to 31 mg·cm^2 (Table S1). The obtained "raw" EIS data sets are shown in Fig. S10 which shows that the impedance at all three voltages decreases with increasing NMC mass in the cathode—i.e. the impedance tail becomes shorter and the impedance arc at medium frequencies becomes smaller. Further details are difficult to recognize from Fig. S10, as the impedance values lie in a wide range and the spectra intersect and overlap considerably at high and medium frequencies. Nevertheless, it is important to note that at all three voltages, the length of the low-frequency tail, |Im(Z)|, decreases continuously as the mass of the NMC in the cathodes increases. Figure 7 shows the corresponding set of mass-normalized EIS spectra of NMC-Li cells in the frequency range from 1 MHz down to 0.1 mHz. It can be clearly seen in Fig. 7 that the normalized impedance tail (i.e., the magnitude of $\mathrm{Im}(Z)_m$) at the lowest frequency (0.1 mHz) directly reflects the nearly ideal parallel coupling of the contributions to the total chemical capacitance of the NMC material in the cathodes. Indeed, we find that the magnitude of $\mathrm{Im}(Z)_m$ at 0.1 mHz depends only slightly on the NMC mass loading. More precisely, $\mathrm{Im}(Z)_m$ increases slightly with increasing mass loading; a linear fit (red dashed line) gives the following values at the small mass end: 1.42 Ω· g at 3.665 V, 1.55 Ω· g at 3.805 V, and 2.26 Ω· g at 4.055 V. We will come back to these values later when we discuss the chemical capacitance and the differential capacity of the cathodes.

As described above, mass normalization applies exclusively only to the transport/reaction processes coupled in parallel. Accordingly, pure series contributions (e.g. the high-frequency intercept, which mainly corresponds to the electrolyte migration resistance in a separator) do not need to be analyzed as part of mass normalization[c]. Since pure series contributions are connected in series with the other contributions the shape of the impedance spectrum remains the same after mass normalization. At this point, we will not focus on the series contributions—accordingly, we can make arbitrary shifts in Re(Z) of the normalized EIS spectra. To compare the interfacial response of the cathode, we have slightly shifted the real parts of the EIS spectra in Fig. 7 so that the corresponding impedance arc of the cathodes is aligned at the "saddle point" of the transition from interfacial impedance to low-frequency diffusion features, as shown in the zoom-in plots in Figs. 7b, 7d, 7f.

At high frequencies, Fig. 7 shows an impedance arc which is due to the interfacial response of the Li metal anode.[11] With increasing mass loading of the NMC cathode, the current density at the Li anode (current per geometric area of the anode) increases during the cycling in proportion to the loading. Consequently, the effective surface area of the pre-cycled Li anode also increases[33]—although the relationship is not simply proportional. In the tested range from the smallest to the largest cathode loading (from 0.7 to 31 mg·cm^{-2}) with corresponding charges from 0.3 to 6.2 mAh·cm^{-2}, the peak frequency of the Li anode arc decreases slightly from about 1.5 kHz (for the smallest loadings) to 500 Hz (for the largest loadings).

To verify the contribution of the Li anode to the EIS of the NMC-Li cells, we galvanostatically cycled symmetric Li-Li cells at different current densities, mimicking the pre-cycling step of the NMC-Li cells. The obtained EIS spectra of the precycled symmetric Li-Li cells are shown in Fig. S11. It was suggested that the Ni-rich NMC cathode has little effect on the cycling (and EIS evolution) of the Li metal anode,[39] so accordingly one half of the EIS response of a Li-Li cell could in principle serve as a good estimate of the impedance response of the Li anode in the NMC-Li half cells. Fig. S11 shows that the peak frequencies of the interfacial high-frequency arc (H.F.-arc) of the Li-Li cells match those of the NMC-Li cells (Fig. 7). Moreover, as expected, the magnitude of the interfacial high-frequency arc (ion migration in the pores of the deposited Li + SEI resistance) decreases with increasing current during cycling—in agreement with the reported data.[33]

The second impedance arc with a well-defined peak frequency of about 20 Hz is due to the interfacial contribution of the NMC particles and its size ($\mathrm{Re}(Z)_m$) is only weakly dependent on the cathode mass loading—in agreement with the theoretical predictions

[c]For example in the case of electrolyte ion migration resistance (in separator) measured at high frequencies, R_{el}, mass normalization produces simple scaling effect. Concretely, for a defined separator material, geometry, type and amount of electrolyte, temperature, and applied pressure (force) the magnitude of R_{el} should be independent of cathode mass loading and having a constant value. Mass-normalization of R_{el} effectively shifts Re(Z) to the value of $R_{el}\bullet m$ that does not have a definite physical meaning.

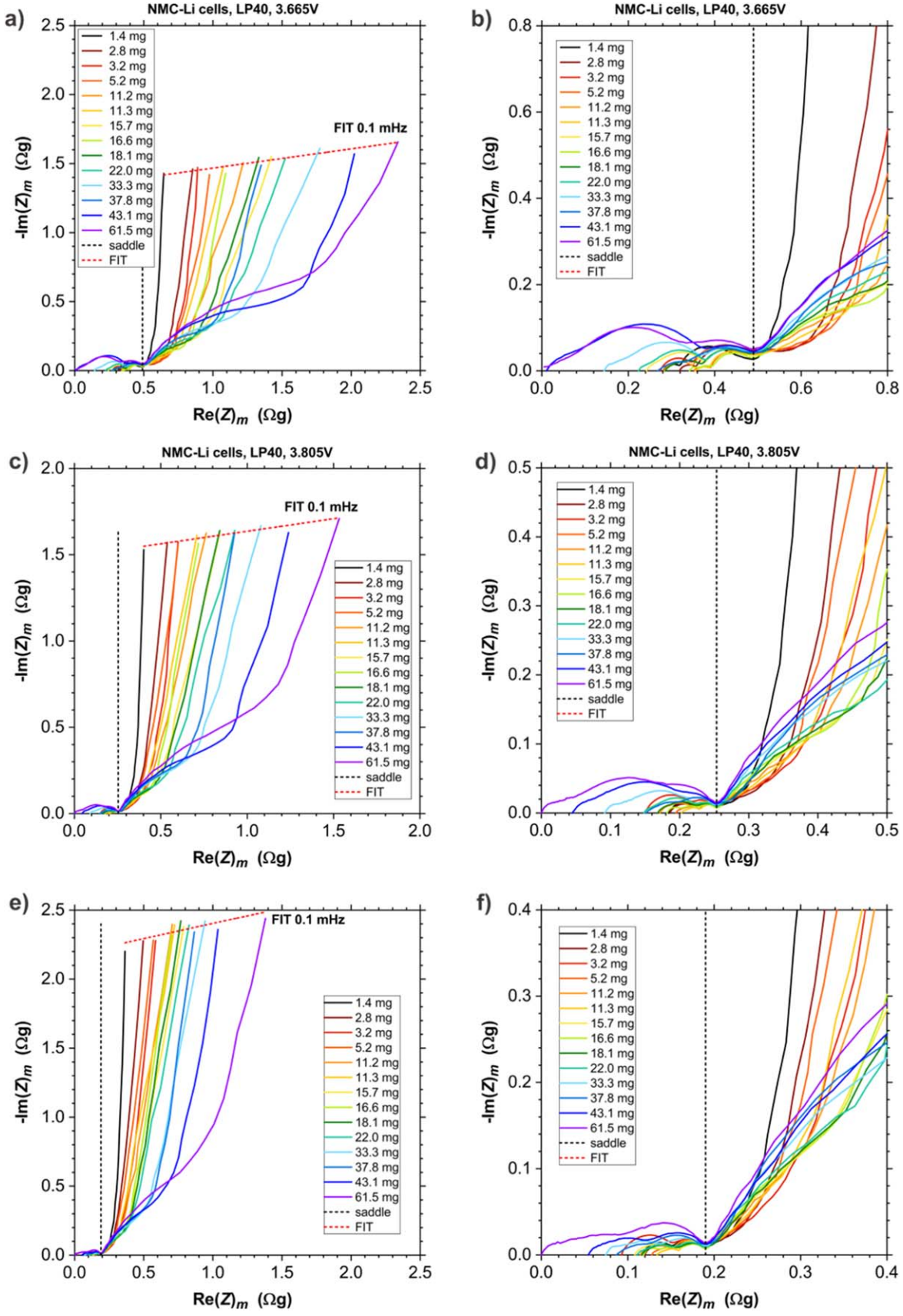

Figure 7. Mass-normalized EIS spectra of set of 14 NMC-Li cells with cathodes with different NMC mass loadings from 0.7 to 31 mg·cm^{-2} at 3 selected voltages: (a-b) $V_1 = 3.665$ V, (c-d) $V_2 = 3.805$ V, and (e-f) $V_3 = 4.055$ V. The Re(Z) of the spectra are aligned at the "saddle point."

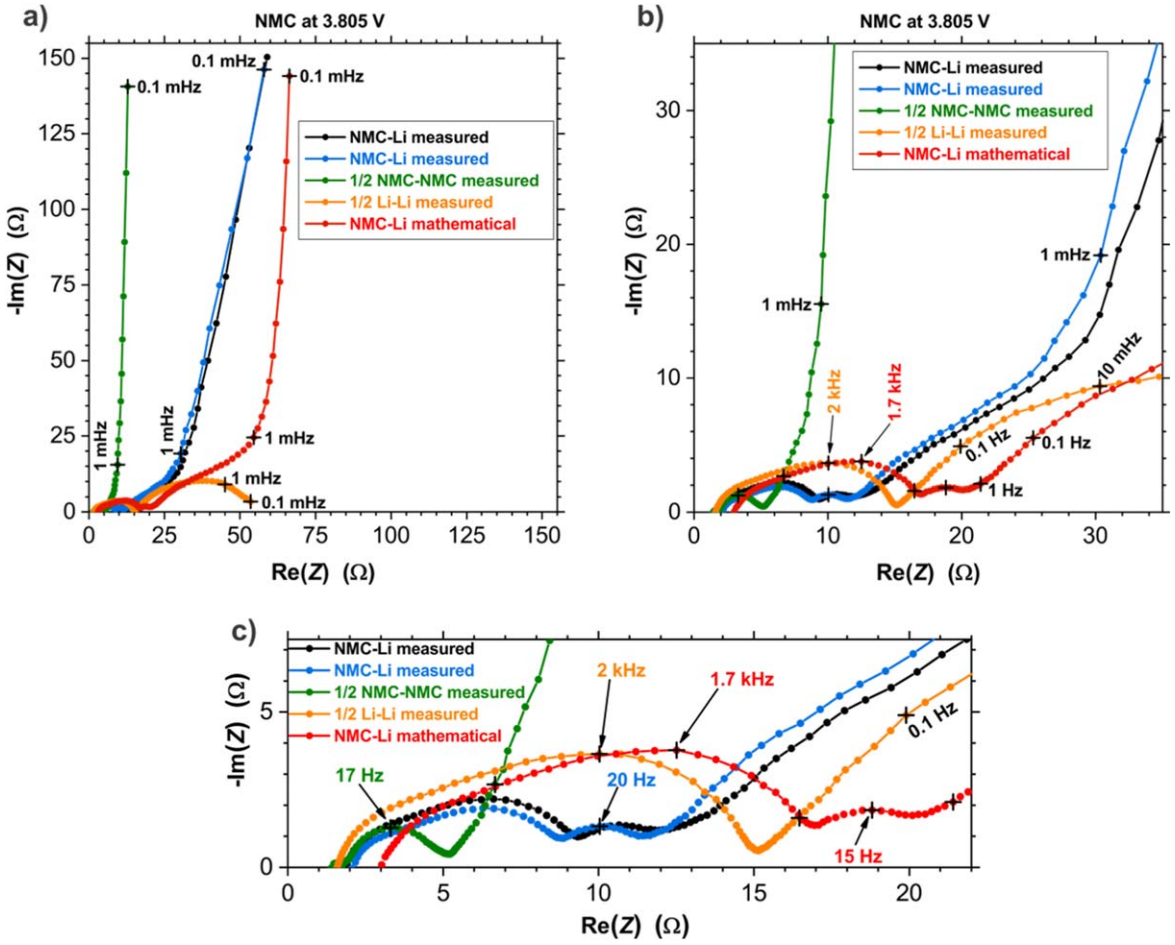

Figure 8. A typical example of a selected set of EIS spectra of the two "parent" (starting) NMC-Li cells and the corresponding secondary NMC-NMC (1/2) and Li-Li (1/2) cells for NMC cathodes equilibrated at 3.805 V; for comparison it is also shown mathematical sum of the impedances of the symmetric cells (1/2 Li-Li + 1/2 NMC-NMC, labeled as "mathematical NMC-Li"). The spectra are shown in: (a) entire frequency span, (b) at medium frequencies, and (c) high frequency part, respectively; the mass of NMC was about 11 mg (mass loading 5.5 mg·cm^{-2}).

in which it was shown that this arc is dominated by the charge incorporation resistance (R_{CT}) at the NMC-electrolyte interface.[12] A more detailed description of this medium-frequency arc contribution can be found in the continuation, in which we discuss the EIS of symmetric NMC-NMC cells.

The impedance contributions in the NMC-Li cells at low frequencies after the "saddle point" transition (at 2–3 Hz) are associated with the various diffusional processes.[12,13] A brief examination shows a pronounced low-frequency hump (in the range from ca. 1 Hz to 1 mHz), followed by a CPE-like (tilted) impedance tail (from about 1 mHz down to $f_{min} = 0.1$ mHz). However, a precise analysis of these characteristics is very complex and is not attempted in the present work. One of the main objectives of the present work is solely to resolve and analyze the individual diffusional contributions in NMC cathodes. Therefore, we give here only a brief description of the obtained EIS spectra. In particular, the total mass-normalized diffusional resistance, $R_{diff}(\text{total})_m$, increases with the mass of the NMC in the cathodes (Fig. 7). Intuitively, one could simply attribute the observed increase in $R_{diff}(\text{total})_m$ directly to the sought-after effect of the increased cathode thickness. Furthermore, one could use the parameters of the active cathode material parameters and the parameters of the electrode geometry to calculate, for example, the solid-state chemical diffusion coefficient of Li in the investigated NMC material. We show in the continuation that such an attempt would be futile.

The EIS spectra of symmetric Li-Li cells shown in Fig. S11 show that, in addition to the influence of current density on the high-frequency arc, there is also a strong influence on the medium- to low-frequency range, where the diffusion of Li-salt in the electrolyte is measured within the deposited high-surface area Li. Furthermore, we see that differences are also observed at very low frequencies where an extended suppressed resistive arc feature is observed with peak frequencies in the mHz range, which is consistent with previous work.[11] It is interesting (and more accurate) to compare the spectra of NMC-Li cells with the corresponding spectra of symmetric NMC-NMC and Li-Li cells obtained from these very NMC-Li cells. A typical example of a selected set of EIS spectra of the two initial NMC-Li cells and the corresponding secondary NMC-NMC (1/2) and Li-Li (1/2) cells is shown in Fig. 8. It is important to note that the overall diffusion resistance of the NMC-Li cells is dominated by the contributions from the (cycled) anode. So we see that the (cycled) Li anode strongly influences the real part of the impedance response of the NMC-Li cells in the entire tested frequency range down to 0.1 mHz. Moreover, surprisingly, we find that the simple mathematical addition of the impedances of the symmetric cells (1/2 Li-Li + 1/2 NMC-NMC) does not reproduce the spectrum (1 mHz–0.1 mHz) of the NMC-Li cells. For example, the slope of the low-frequency impedance tail of the NMC-Li cells is significantly lower than that measured for the NMC-NMC cell and calculated for the "mathematical" NMC-Li cell. The reason for this deviation is currently unclear and will be part of our future research work. Importantly, an attempt to use the CPE-like frequency dependence of the impedance tail of NMC-Li cells directly to analyze the resistive contributions of NMC cathodes would clearly lead to overestimated values. Interestingly the imaginary component (Im(Z)) of the impedance tail is much less affected by the presence of (cycled) Li anode. This last observation

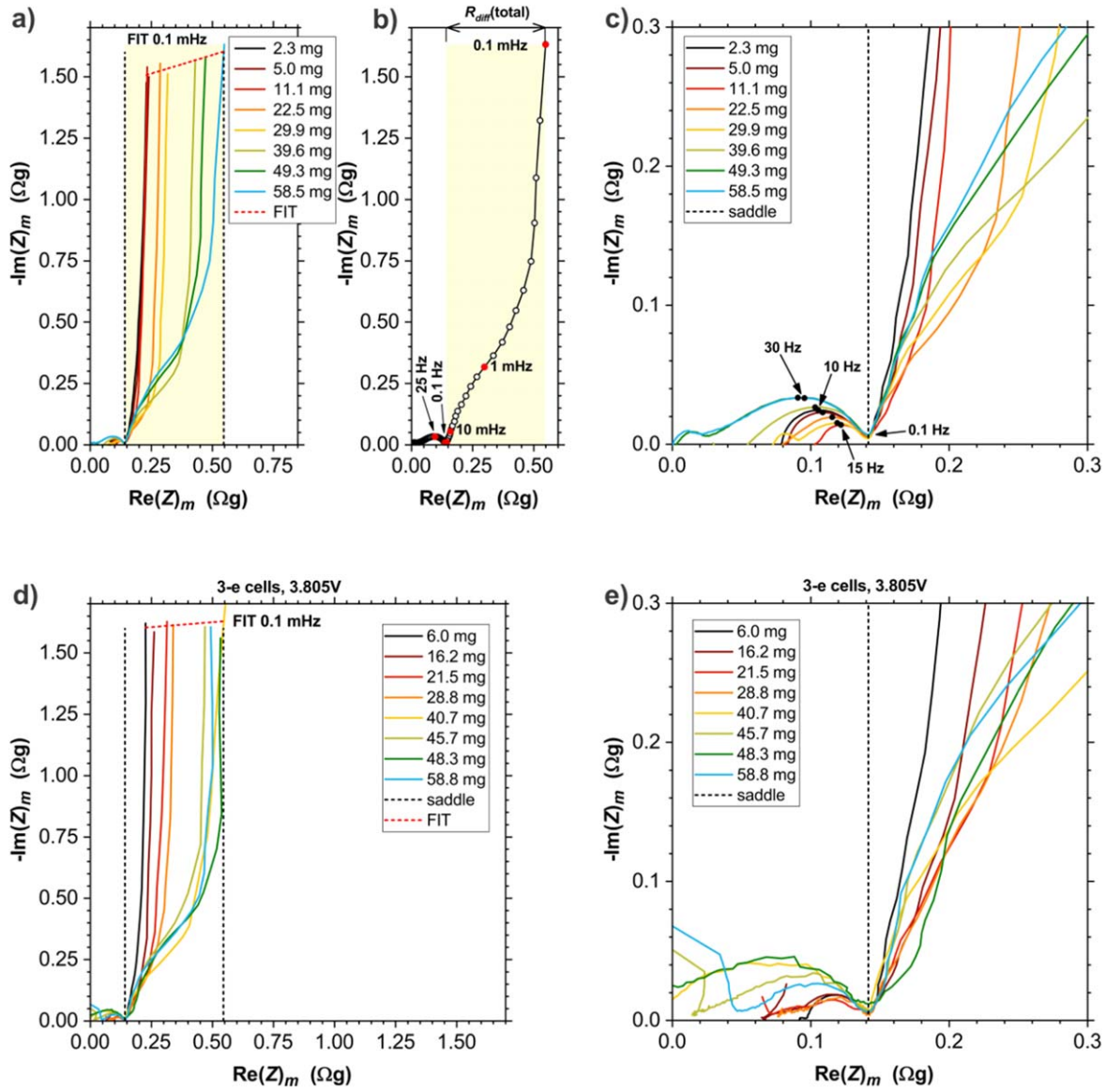

Figure 9. Mass-normalized EIS spectra of series of: (a-c) 8 symmetric NMC-NMC cells with cathodes with different NMC mass loadings (from ~1.2 to 29 mg·cm^{-2}); (d-e) 8 NMC||RE(Au-Li)||CE(Li) 3-electrode cells with cathodes with different NMC mass loadings (from 3 to 29 mg·cm^{-2}). All spectra were measured at the selected voltage $V_2 = 3.805$ V. The Re(Z) of the spectra are aligned at the "saddle point."

indicates that mass normalization can be applied to half-cells (of course, only if the EIS spectra are measured down to a sufficiently low frequency, e.g. 0.1 mHz).

A further detailed analysis of the EIS spectra of the NMC-Li cells compared to the Li-Li cells is not attempted here, as this is not relevant to the present study. **PART-2** of this study will discuss in more detail the misleading results that can arise when attempting to perform an analysis of diffusional contributions of the NMC cathodes directly from the EIS data of the NMC-Li cells.

Measured sets of EIS spectra of symmetric NMC-NMC cells and 3-electrode cells with cathodes (at 3.805 V) with different mass loadings.—With the aim of removing the described contribution of the (pre-cycled) Li anode, we prepared two sets of cells with cell configurations that should allow (at least in principle) to precisely measure only the desired response of an inspected electrode. For this purpose, we applied two approaches: (a) the long-known symmetric cell approach, which is now widely used in this field,[40–43] and (b) the three-electrode setup with gold wire micro-reference electrode (GWRE), which has been proposed in recent years.[44–46] Further technical details on the preparation of the cells used in the present work can be found in Experimental. In brief, a symmetric pouch-type NMC-NMC cell was prepared from a pair of nominally identical cathodes, pre-cycled using the same procedure as the NMC-Li cells and brought to the selected voltage $V_2 = 3.805$ V, where they were equilibrated during a voltage hold. In this way, we prepared a set of 8 symmetric NMC-NMC cells and measured the EIS response in the frequency range from 1 MHz down to 0.1 mHz. The obtained mass-normalized spectra are shown in Figs. 9a–9c.

A pouch-type three-electrode NMC||RE||Li cell was prepared from an NMC cathode, a Li metal anode, and an insulated GWRE with an inner diameter of 50 μm between two glass fiber separators. The gold wire was pre-prepared by carefully removing about 300 μm of the insulating layer. After assembling the cell, we first performed galvanostatic lithiation of the GWRE with the Li anode serving as the lithium source. We performed a 2-electrode precycling of an NMC cathode and then brought it to the selected voltage $V_2 = 3.805$ V, where it equilibrated during a voltage hold (for details, see Experimental). This way, we prepared a set of 8 NMC||RE(Au-Li)||CE(Li) 3-electrode cells and measured the EIS response in the frequency range from 1 MHz down to 0.1 mHz. The obtained mass-normalized spectra are shown in Figs. 9d–9e. As with the NMC-Li

cell sets, we aligned Re(Z) of the EIS spectra to the "saddle point" where the low-frequency diffusion processes start (see explanation in the previous section).

The EIS spectra of the symmetric NMC-NMC cells in Figs. 9a–9c only contain the (desired) impedance response of the investigated cathodes and the response of the electrolyte-soaked separator. Examining the medium- and low-frequency part of the spectra in Figs. 9a–9c, we find three main important observations: (a) the magnitude of $\mathrm{Im}(Z)_m$ of the low-frequency tail at 0.1 mHz shows an almost constant value, and (b) the magnitude of $\mathrm{Re}(Z)_m$ in the medium- and low-frequency (diffusional) region is greatly reduced compared to the corresponding values obtained for the set of NMC-Li cells, and (c) the magnitude of $\mathrm{Re}(Z)_m$ in the diffusional region increases with increasing NMC mass loading. Since there are no contributions from the Li anode (counter electrode) in the EIS spectra in Figs. 9a–9c, the observed effects are solely due to the effects of finite cathode thickness. This is because as the NMC mass loading of the electrode increases, we simultaneously increase the cathode thickness (Table S2), thus increasing the effective path for diffusion of lithium to the surface of the active NMC particles (aggregates). Accordingly, the total diffusional resistance, R_{diff}(total), which is read off in Fig. 9b as the distance between the "saddle point" and Re(Z) at 0.1 mHz, corresponds to the sum of the contributions of the diffusional resistances: (i) in the electrolyte-filled pores within the cathode, (ii) in the solid-state within the NMC active material aggregates, and (iii) in the (half) separator.

One should get the same or at least very comparable information from the series of EIS spectra of 3-electrode cells (Figs. 9d–9e). And indeed, we see that the diffusion part of the spectra is quite comparable to the spectra of the corresponding symmetric cells (note that in the spectra of the symmetric cells, e.g. in Figs. 9a–9b, the magnitude of the impedance corresponds to a single cathode). Thus, the approach based on the use of 3-electrode cells with GWRE actually provides EIS spectra of quite good quality in the diffusion region. On the other hand, the 3-electrode approach has a certain disadvantage in terms of the quality of the high- and medium-frequency part of the spectra. As can be seen in Figs. 9c and 9e**,** impedance measurements in the 3-electrode setup (in addition to the high-frequency artifacts) lead to a larger measurement noise in the obtained EIS data[46] compared to the measurements on symmetric NMC-NMC cells.

Figures 9c and 9e show that the size of the mass-normalized impedance arc of the NMC cathode tends to increase with increasing NMC loading, while the peak frequency increases from 10 Hz to about 30 Hz. At low loadings (thicknesses), the arc is dominated by the contribution of the charge incorporation resistance (R_{CT}). With increasing cathode thickness (at constant porosity and tortuosity) the resistance due to ion migration in the cathode pores increases proportionally—observed as the inclined (by about 45 degrees) left part of the arc. Eventually, this resistance starts to dominate over R_{CT} in the thickest cathodes—as analyzed and discussed in **PART-2**. The described effect of electrode thickness on the size and shape of interfacial arc where there is interplay between R_{CT} resistance and ion migration resistance in electrode pores was very clearly demonstrated and explained in work by Morasch et al.[47]

The observed slight increase in $\mathrm{Im}(Z)_m$ with mass (electrode thickness) reflects the fact that not all NMC storage particles are at exactly the same potential (and in the same phase) when measuring the impedance response of thick cathodes, even at frequencies as low as 0.1 mHz. And with increasing thickness, this becomes even more pronounced. Overall, this is the expected effect of electrode thickness (mass loading), as explained in the continuation and analyzed in detail in PART-2. A linear fit of the impedance points at 0.1 mHz of the aligned spectra of the NMC-NMC cells at 3.805 V (red dashed line, Fig. 9d) gives the value of $\mathrm{Im}(Z)_m$ of 1.51 Ω· g at the small mass end. The corresponding value of the NMC-Li cells (Fig. 7c) was slightly larger (1.55 Ω· g) due to the small contribution of the Li anode to $\mathrm{Im}(Z)_m$. The former value is related to the actual intrinsic charge storage capacity of the investigated NMC insertion material at 3.805 V, as explained in the following sections. Recently, Morasch et al.[27] reported a similar type of analysis for NMC111, but with the important difference that they performed EIS measurements only down to 1 mHz; a further comparison and discussion of the results can be found in the following section (Fig. 12).

Quantitative relation between differential capacity, C_d, and low-frequency part of Im(Z).—In addition to the suggestions for "mass normalization scaling" of the low-frequency part of Im(Z) of the EIS spectra (see section "Mass-normalization of EIS spectra"), it was established (recognized) early on that there is a clear correlation between the differential capacity, C_d, and the magnitude of the low-frequency part of Im(Z) of the tested electrode. Indeed, it was generally confirmed that the minima of |Im(Z)| are closely aligned with the maxima of C_d.[36] By combining these two empirical relationships and using the (idealized) assumption of "perfect" capacitive storage[48] in the insertion material,[27,49] one can construct simple intuitive (hypothetical) quantitative relationship that defines the total EIS capacitance of an electrode, C_{total}:

$$\frac{C_{total}(x)}{m} = \lim_{f\to 0}\left\{\frac{1}{i\omega \cdot Im(Z)_m}\right\} = \lim_{f\to 0}\left\{\frac{C^{\delta}_{ins}(x,\,\omega)}{m}\right\} = \theta\frac{C_d(x)}{m}, \qquad [2]$$

where ω is the angular frequency ($\omega = 2\pi f$), $C_d(x)$ stands for the differential capacity of the cathode[50] and θ is a capacity utilization factor that ranges from 0 to 1 and indicates what fraction of $C_d(x)$ can actually be achieved during the impedance perturbation for a given x. Please note that in Eq. 2 the parameter θ is defined for the the zero-frequency condition. For the ideal case of a single-phase solid-solution lithiation of AM particles, a value of θ of 1 (100%) is expected. The value of θ must be determined experimentally and cannot formally exceed 1.

The above relation is expected if one assumes that the diffusive (insertion) charge storage exhibits an (almost) purely capacitive response and simultaneously (and uniformly) varies the concentration throughout the volume of the active material when subjected to a perturbation at a sufficiently low frequency. For an insertion electrode in equilibrium (state defined by x, see section "Impedance measurement methodology"), we naturally expect it to exhibit a linear behavior only locally (near x). In other words, the amplitude of perturbation should be small enough so that the corresponding storage capacitance C_d is close to constant (Fig. 10a) and the frequency low enough so that all the active material in the electrode is probed at (almost) identical phase of the input signal. The above relation is formally "derived" in PART-2 when we consider general scaling relations of the equivalent transmission line (TL) model. The question is whether it is possible to experimentally investigate the zero-frequency boundary conditions of insertion diffusional storage according to Eq. 2. If so, then the corresponding value of the total normalized capacitance ($C_{total}(x)/m$, in F per 1 g AM) and θ could be obtained directly from the corresponding mass-normalized Nyquist plots and known C_d. Figure 10a shows the experimentally determined OCV dependence plotted as x vs NMC electrode voltage measured in a well-controlled GITT experiment on a 3-electrode NMC||RE(Li)||CE(Li) cell at controlled temperature (24.0 ± 0.1 °C) (see Fig. S12, details under Experimental). Let us turn our attention for example to the state at 3.805 V where we observe in the corresponding magnified part (inset in Fig. 10a) that the slope of the curve on the segment within the input perturbation signal (+/−5 mV) is very close to the constant. A closer examination (Fig. S13) revealed a standard deviation of the slope of slope the curve of 0.06%; in this particular case, the deviation from linearity is therefore less than 0.1% (estimated). When measuring the impedance in the selected state (3.805 V) by applying an input amplitude of 5 mV at 0.1 mHz, the amplitude of the output current response (δI) corresponds approximately to the C/80 rate (relative to the theoretical capacity of 275 mAh g^{-1}).

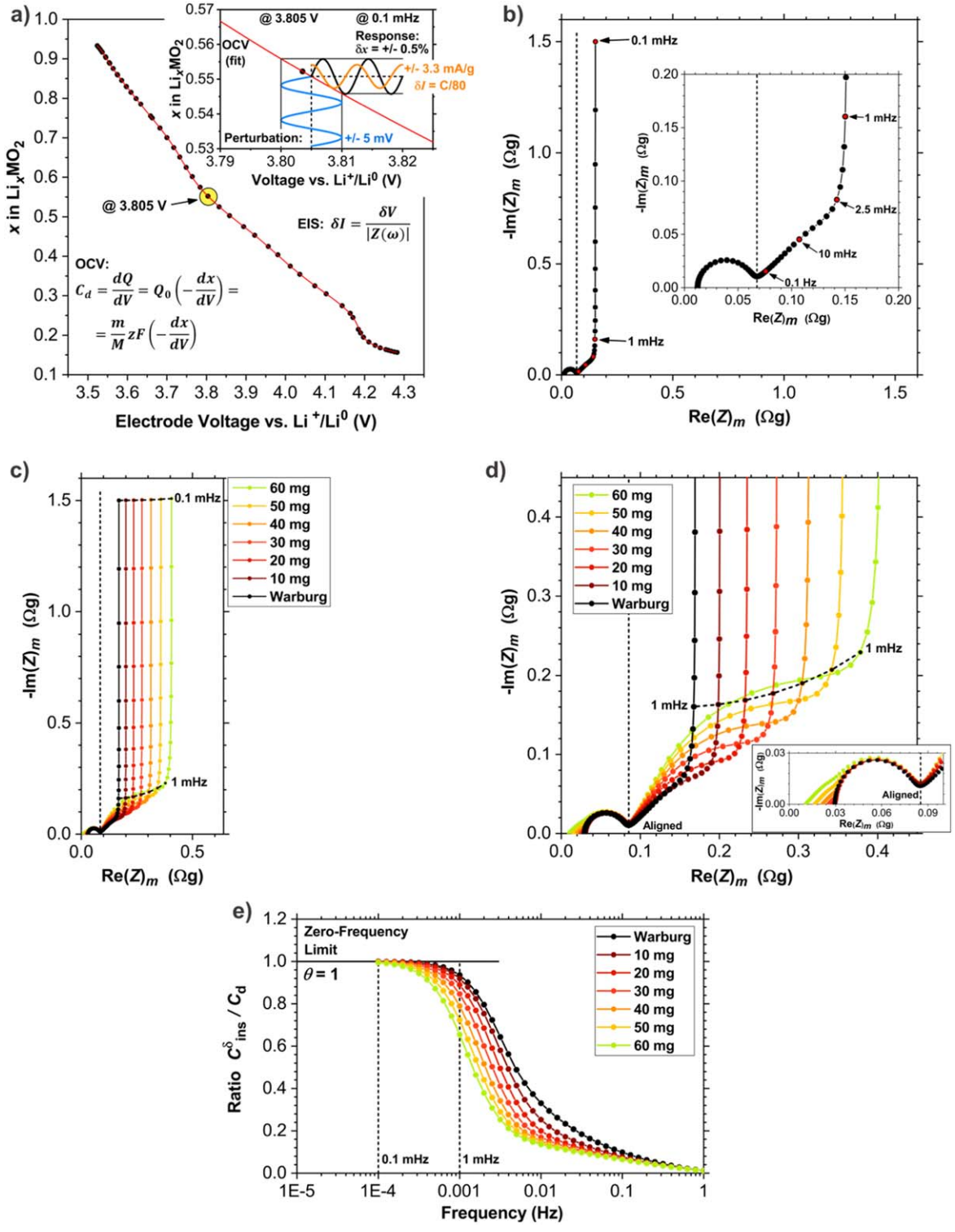

Figure 10. (a) Experimentally determined OCV dependence plotted as x vs NMC electrode voltage measured in a well-controlled GITT experiment. (b) EIS response of an ideal Warburg (open) element combined with interfacial R_{ct}. (c–d) An illustration of the application simple analysis based on the assumption of an ideal capacitor (Eq. 2) to obtain the total storage capacitance C_{total}. For simplicity the ideal Warburg (open) was used to represent the solid-state diffusional storage in AM. In addition, the diffusion in the (half) separator and in the porous electrode was included in the simulations for the range of NMC masses in the cathode (the values of the parameters are consistent with the results obtained in PART-2). (c) Set of simulated mass-normalized EIS spectra in the whole frequency range (1 MHz—0.1 mHz), and (d) Enlarged view of the medium-frequency range with the characteristic "knee" transition dropping from about 2.5 mHz (ideal Warburg) to about 1 mHz for the thickest electrode (NMC mass 60 mg, loading 30 mg·cm^{-2}, geometric electrode area 2 cm^2). (e) According to Eq. 2, the determination of the C_{total}/m is equivalent to finding the limiting asymptote of $C^{\delta}_{ins}(x, \omega)/m$ when the frequency approaches to zero. In the zero frequency limit, the ratio is $C^{\delta}_{ins}/C_d = C_{total}/C_d$ and is equal to the capacity utilization factor θ (which was set to 1).

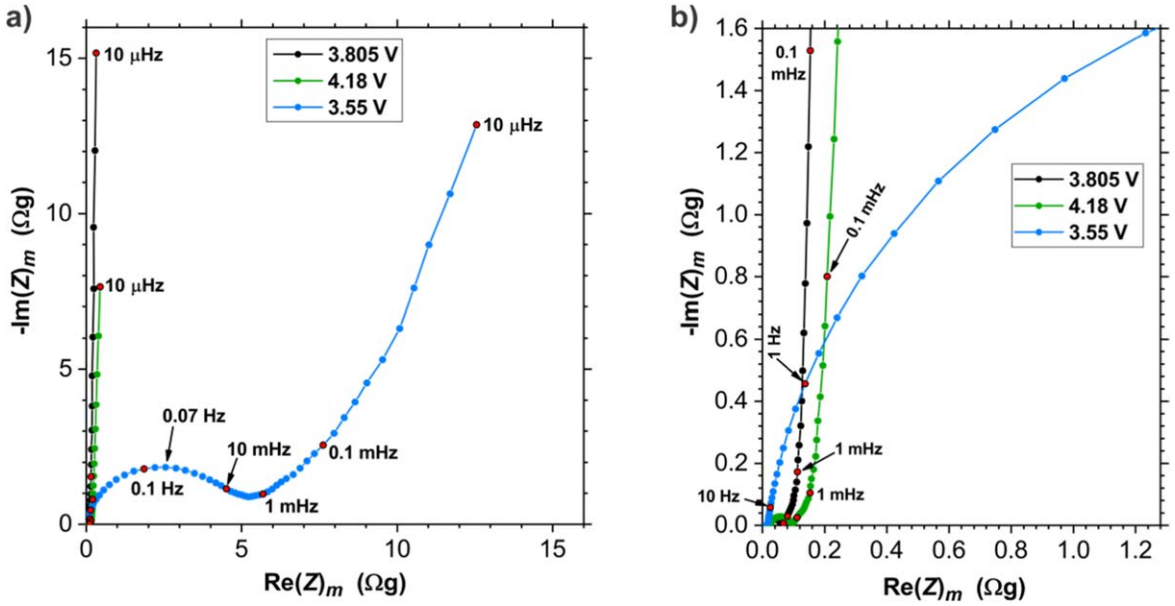

Figure 11. EIS spectra of NMC-NMC cells measured down to an extremely low frequency (10 μHz) at three selected states: (i) 3.805 V (black), (ii) 4.18 V (green), and (iii) 3.55 V (blue). Electrode geometric area was 2 cm^2 and the corresponding masses of NMC in the electrodes were: (i) 10.8 mg, (ii) 11.7 mg, and (iii) 11.4 mg, respectively.

The differential capacity C_d is proportional to the slope of the x vs voltage curve: $C_d = \frac{dQ}{dV} = Q_0\left(-\frac{dx}{dV}\right) = \frac{m}{M}zF\left(-\frac{dx}{dV}\right)$, where Q_0 stands for the charge stored in the electrode. Mass normalization provides a simple expression, which in the specific case of the state at 3.805 V reads: $\frac{C_d}{m} = \frac{zF}{M}\left(-\frac{dx}{dV}\right) = \frac{1{\cdot}96485\text{As}{\cdot}\text{mol}}{97.43\ \text{g}{\cdot}\text{mol}}(1.055\ \text{V}^{-1}) =$ 1045 F/g. The value of $\left(-\frac{dx}{dV}\right)$ was determined from the derivative of the fitting curve (red line) to the experimental OCV points (black circles) shown in Fig. 10a at the selected voltage. The total capacitance (C_{total}) is obtained from the imaginary part of the corresponding low-frequency part of the impedance spectrum ("capacitive tail") as follows. For clarity, we can compare the simplest and well-defined case of an insertion storage response of a pure 1D (open) Warburg element combined only with interfacial R_{ct} (Fig. 10b). It is important to note the "knee" transition point from the distinctive 45° slope into a vertical capacitive "tail"; in the specific case in Fig. 10b**,** the transition is at about 2.5 mHz. We have simulated a series of EIS spectra with additional contributions from diffusion in the (half) separator and in the the porous electrode for s range of NMC masses in the cathode, using parameter values consistent with the results obtained in PART-2. The obtained EIS spectra in the whole frequency range (1 MHz–0.1 mHz, Fig. 10c) show a gradual shift of the capacitive tail towards larger Re(Z) due to the increasing combined contributions of both additional diffusional processes in the liquid electrolyte phase—observed as a medium-frequency "hump" (Fig. 10d). We find that as the size of the hump increases (increasing NMC mass/electrode thickness), the characteristic "knee" transition frequency gradually decreases from 2.5 mHz (ideal Warburg) to about 1 mHz for the thickest electrode (NMC mass 60 mg, loading 30 mg·cm^{-2}, geometric electrode area 2 cm^2). At the same time, the magnitude of Im(Z)$_m$ at 1 mHz gradually increases while the increase of Im(Z)$_m$ at 0.1 mHz is very small.

In Fig. 10e the ratio C_{ins}^{δ}/C_d is shown and for a certain frequency, we find that the ratio gradually decreases with increasing NMC mass (loading). For example, at 1 mHz, we find that the electrode simulated with the ideal Warburg element has a ratio of 0.935, while the 60 mg electrode (loading 30 mg·cm^{-2}) has only 0.654. On the other hand, the ratio at 0.1 mHz is much closer to unity, with the ideal Warburg electrode having 0.9997, while the thickest 60 mg electrode has 0.994. In the zero frequency limit, the ratio C_{ins}^{δ}/C_d is equal to the capacity utilization factor θ, which was set to be exactly 1 by simulation conditions (for all simulated electrodes C_{total} was kept constant and is equal to C_d).

We have verified the validity of the proposed Eq. 2 by performing impedance measurements on NMC-NMC cells down to extremely low frequencies (10 μHz). Figure 11 shows the obtained EIS spectra at three selected states corresponding to: (i) 3.805 V (central composition), (ii) 4.18 V (composition with plateau-like behavior associated with the phase separation,[30] and (iii) 3.55 V (composition with high degree of lithiation, x estimated at 0.90).

We note that the spectra measured at 3.805 V and 4.18 V show the expected capacitive response at low frequencies. In contrast, the spectrum measured at 3.55 V deviates strongly—both the interfacial and diffusion resistance are much larger compared to other (tested) compositions. Furthermore, it is clear that at 3.55 V the applied perturbation with a frequency of only 10 μHz is not low enough to observe a purely capacitive response. Figure 12 shows the results of analyzing the EIS spectra by applying the relationship[6] and Eq. 4 to the measured impedances of the NMC-Li and the NMC-NMC cells (at V_1, V_2 and V_3, lowest frequency 0.1 mHz) and the NMC-NMC cells measured to 10 μHz (at V_2, V_4 and V_5). The differential capacity of the NMC cathode, $C_d(x)$, was determined from the OCV dependence (Fig. 12b), which was measured in a well-controlled GITT experiment on a 3-electrode NMC||RE(Li)||CE(Li) cell at controlled temperature (24.0 ± 0.1 °C) (see Fig. S12).

Figure 12a shows that the (storage) capacitance of the NMC electrode as a function of frequency, which results from Eq. 4 (ideal capacitor), is strongly dependent on the NMC mass loading (thickness). As expected, the capacitive storage shifts towards lower frequencies as the NMC loading (thickness) increases, which is consistent with the results of Morasch et al.[27] This observation is actually the impedance reflection of a more general statement: as the electrode thickness increases, the effective time required to change the (average) lithiation level of an AM for a given Δx increases accordingly due to the corresponding contribution of the increased delay time. For the specific set of EIS data (Fig. 12a) the individual contributions to the "lag time" are analyzed in **PART-2**.

Figure 12b shows three examples of the determination of the total NMC cathode capacitance, $C_{\text{total}}(x)$, from EIS spectra of NMC-NMC

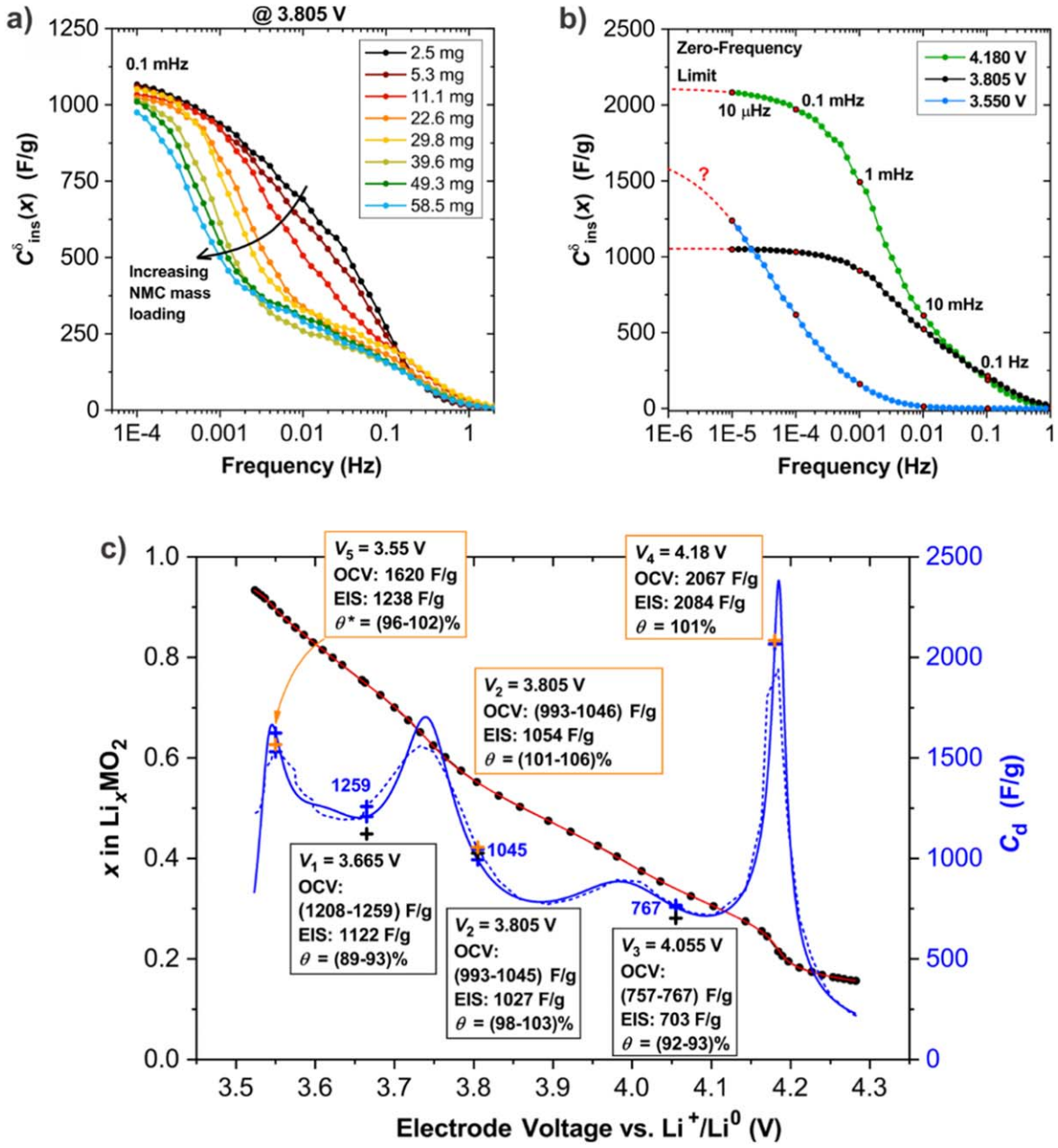

Figure 12. NMC electrode capacitance as a function of frequency determined with Eq. 2 (ideal capacitor) for the following cells: (a) NMC-NMC cells with increasing NMC mass loading equilibrated at 3.805 V and measured down to 0.1 mHz (see Fig. 9), (b) NMC-NMC cells equilibrated at: (i) 3.805 V (black), (ii) 4.18 V (green), and (iii) 3.55 V (blue) and measured down to 10 μHz; the corresponding masses of NMC in the electrodes were: (i) 10.8 mg, (ii) 11.7 mg, and (iii) 11.4 mg. c) Experimental dependence of x vs OCV for the Ni-rich NMC obtained in a dedicated GITT experiment (Fig. S12) with the actual measured equilibrated points (black circles) and the best fit curve (polynomial of degree 12, red line). Comparison of the total electrode capacitance, $C_{\text{total}}(x)$, obtained from the EIS spectra of NMC-NMC cells measured down to 0.1 mHz (black +) and down 10 μHz (orange +) by using Eq. 2. The values of $C_{\text{total}}(x)$ are shown in relation to the corresponding differential capacity of the NMC cathode, $C_d(x)$, obtained from fitting the OCV dependence (blue line, blue +) and the actual set of measured OCV points (blue dashed line, blue +). The results obtained for the parameter θ are more reliable in the case of EIS measurements down to 10 μHz (with the exception of the value of θ at 3.55 V, which was obtained by an assumed extrapolation curve, see Fig. 12b). The OCV dependence was measured on 3-electrode NMC||RE(Li)||CE(Li) cell. In all cases, the geometric surface area of the NMC electrode was 2 cm^2.

cells equilibrated at 3.805 V, 4.18 V, and 3.55 V and measured down to 10 μHz. In Fig. 12b we can see in that in the case of the NMC cathodes at 3.805 V and 4.18 V, the determination of $C_{\text{total}}(x)$ is possible since the true low-frequency limit can be obtained by extrapolation, resulting in 1054 $F{\cdot}g^{-1}$ and 2084 $F{\cdot}g^{-1}$, respectively. However, in the case of the NMC cathode equilibrated at 3.55 V, the determination of $C_{\text{total}}(x)$ is not possible; we can only determine that the value of $C_{\text{total}}(x)$ is greater than 1238 $F{\cdot}g^{-1}$. In the specific case of NMC83-06-11, which was equilibrated at 3.55 V, the corresponding time constant for solid state diffusion ($\tau^{\delta} = R^{\delta}C^{\delta}$) is extremely large (definitely greater than 28 hours) and therefore cannot be measured (instrumental limitation at 10 μHz). Figure 12c shows the comparison of $C_{\text{total}}(x)$ from the EIS at 0.1 mHz and 10 μHz and the corresponding differential capacity of the NMC cathode, $C_d(x)$, obtained from the precise OCV dependence. Specifically, Fig. 12c shows the experimentally determined dependence of x vs OCV for the Ni-rich NMC from a dedicated GITT experiment (Fig. S12) with the actual measured equilibrated points (black circles) and the best fit curve (polynomial of degree 12, red line).The $C_d(x)$ curve vs x (voltage) was obtained from the experimental equilibrium OCV

dependence by the procedure described above (see description of Fig. 10a) from the best fit of the OCV dependence (blue line) and for comparison from the actual set of measured OCV points (blue dashed line). Most importantly, we find that there is a very good agreement between the values of $C_{\text{total}}(x)$ and $C_d(x)$ for all states except at 3.55 V (where C_{total} cannot be determined). To our knowledge, this is the first direct experimental confirmation of the exact validity of a relationship of the type as in Eq. 4 for porous insertion electrodes. In other words, we have experimentally proven that with an impedance perturbation of sufficiently low frequency, we can directly measure the thermodynamic properties of the active insertion material.

Recently Morasch et al.[27] have shown a similar type of comparison for NMC111, but with the important difference that they only performed EIS measurements down to 1 mHz. As can be seen from the present results, the impedance perturbation at a frequency of 1 mHz is definitely not low enough to capture the full storage capacity of NMC cathode materials in porous electrodes. In the present case of the investigated NMC83-06-11, we found that the required lowest frequency is around 0.1 mHz (or even lower, especially for the highly lithiated states of NMC). A similar agreement as in the present study between the OCV-based differential capacity and the impedance-based chemical capacitance was recently demonstrated by Bumberger et al. for thin film cathodes with $LiCoO_2$[51] and $LiMn_2O_4$[52] active materials by applying an approach in which the differential capacity was obtained from cyclic voltammetry. The authors have applied the principles of defect chemistry by creating a defect model to provide a physical interpretation of all fundamental electrochemical properties as a function of SOC, emphasizing the key role of chemical capacitance as an important descriptor of lithium insertion electrode materials.[51]

Conclusions and Outlook

In the present **PART-1**, we have thoroughly characterized secondary particles of Ni-rich NMC active material and corresponding porous electrodes. We have shown which experimental steps are crucial to obtain high-quality impedance data of NMC insertion cathodes. We have outlined several possible scenarios in which one might be tempted to carelessly ascribe a meaning to certain features in the measured EIS spectra, relying on some common misinterpretations. We have demonstrated how mass normalization of Nyquist plots can be used to directly determine the chemical (storage) capacitance, $C_{\text{total}}(x)$, of real (non-ideal) single-phase insertion battery electrodes. Importantly, for Ni-rich NMCs, we directly experimentally confirmed the exact validity of the equivalence of $C_{\text{total}}(x)$ from impedance measurements and the differential capacity, $C_d(x)$, obtained from the exact OCV dependence. In other words: We have shown that impedance measurements performed to sufficiently low frequencies allow the determination of the thermodynamic properties of single-phase insertion active materials in porous cathodes. A detailed and rigorous analysis of the obtained EIS spectra of symmetric NMC-NMC cells (Figs. 9a–9c) can be found in **PART-2**, where the importance and advantages of the scaling relations in the analysis of systematic EIS measurements are demonstrated.

Acknowledgments

Jože Moškon gratefully acknowledges the financial support of the Slovenian Research Agency within the project J2-4463. Sara Drvarič Talian and Robert Dominko gratefully acknowledge the financial support of the Slovenian Research Agency within the national programme No. P2-0423. Miran Gaberšček acknowledges the financial support of the Slovenian Research Agency within the national programme No. P2-0393. Ana Rebeka Kamšek acknowledges the support of the Milan Lenarčič Foundation and the Janko Jamnik Doctoral Scholarship. We thank Marjan Bele for his help and for many fruitful discussions.

ORCID

Jože Moškon https://orcid.org/0000-0002-8223-0031
Sara Drvarič Talian https://orcid.org/0000-0003-1355-2843
Miran Gaberšček https://orcid.org/0000-0002-8104-1693

References

1. K. Zelič, T. Katrašnik, and M. Gaberšček, *J. Electrochem. Soc.*, **168**, 070543 (2021).
2. G. Sikha and R. E. White, *J. Electrochem. Soc.*, **154**, A43 (2007).
3. J. Huang and J. Zhang, *J. Electrochem. Soc.*, **163**, A1983 (2016).
4. J. P. Meyers, M. Doyle, R. M. Darling, and J. Newman, *J. Electrochem. Soc.*, **147**, 2930 (2000).
5. A. Shodiev et al., *J. Power Sources*, **454**, 227871 (2020).
6. W. Lai and F. Ciucci, *Electrochim. Acta*, **56**, 4369 (2011).
7. Y. Fujihara and T. Kobayashi, *J. Electrochem. Soc.*, **169**, 080509 (2022).
8. Q. Zhang et al., *J. Energy Storage*, **50**, 104182 (2022).
9. X. Zhu et al., *J. Power Sources*, **544**, 231852 (2022).
10. S. Drvarič Talian, J. Moškon, R. Dominko, and M. Gaberšček, *Electrochim. Acta*, **302**, 169 (2019).
11. S. Drvarič Talian, J. Bobnar, A. R. Sinigoj, I. Humar, and M. Gaberšček, *J. Phys. Chem. C*, **123**, 27997 (2019).
12. J. Moškon, J. Žuntar, S. Drvarič Talian, R. Dominko, and M. Gaberšček, *J. Electrochem. Soc.*, **167**, 140539 (2020).
13. J. Moškon and M. Gaberšček, *J. Power Sources Adv.*, **7**, 100047 (2021).
14. S. Drvarič Talian, G. Kapun, J. Moškon, R. Dominko, and M. Gaberšček, *J. Electrochem. Soc.*, **169**, 010529 (2022).
15. P. Bankhead et al., *Sci. Rep.*, **7**, 16878 (2017).
16. L. Froboese, P. Titscher, B. Westphal, W. Haselrieder, and A. Kwade, *Mater. Charact.*, **133**, 102 (2017).
17. T. Beuse, M. Fingerle, C. Wagner, M. Winter, and M. Börner, *Batteries*, **7**, 70 (2021).
18. M. Gaberscek, J. Moskon, B. Erjavec, R. Dominko, and J. Jamnik, *Electrochem. Solid-State Lett.*, **11**, A170 (2008).
19. J-M. Atebamba, J. Moskon, S. Pejovnik, and M. Gaberscek, *J. Electrochem. Soc.*, **157**, A1218 (2010).
20. C. Meyer, H. Bockholt, W. Haselrieder, and A. Kwade, *J. Mater. Process. Technol.*, **249**, 172 (2017).
21. H. Liu et al., *Particuology*, **57**, 56 (2021).
22. S. Vierrath et al., *Electrochem. Commun.*, **60**, 176 (2015).
23. C. Schilcher, C. Meyer, and A. Kwade, *Energy Technol.*, **4**, 1604 (2016).
24. F. Friedrich et al., *J. Electrochem. Soc.*, **166**, A3760 (2019).
25. V. Charbonneau, A. Lasia, and G. Brisard, *J. Electroanal. Chem.*, **875**, 113944 (2020).
26. S. Oswald, D. Pritzl, M. Wetjen, and H. A. Gasteiger, *J. Electrochem. Soc.*, **167**, 100511 (2020).
27. R. Morasch, H. A. Gasteiger, and B. Suthar, *J. Electrochem. Soc.*, **170**, 080522 (2023).
28. A. Van der Ven, K. A. See, and L. Pilon, *Batter. Energy*, **1**, 1 (2022).
29. J. Wang et al., *ACS Energy Lett.*, **8**, 2986 (2023).
30. M. Weiss et al., *Adv. Energy Mater.*, **11** (2021).
31. C. Xu et al., *Joule*, **6**, 2535 (2022).
32. P. Bai, J. Li, F. R. Brushett, and M. Z. Bazant, *Energy Environ. Sci.*, **9**, 3221 (2016).
33. Y. Liu et al., *Adv. Sci.*, **8**, 1 (2021).
34. M. GABERSCEK and J. JAMNIK, *Solid State Ionics*, **177**, 2647 (2006).
35. M. Gaberscek, M. Küzma, and J. Jamnik, *Phys. Chem. Chem. Phys.*, **9**, 1815 (2007).
36. M. D. Levi and D. Aurbach, *J. Phys. Chem. B*, **101**, 4630 (1997).
37. D. Aurbach, M. D. Levi, O. Lev, J. Gun, and L. Rabinovich, *J. Appl. Electrochem.*, **28**, 1051 (1998).
38. M. D. Levi and D. Aurbach, *J. Phys. Chem. B*, **108**, 11693 (2004).
39. J. Langdon and A. Manthiram, *Adv. Funct. Mater.*, **31**, 2010267 (2021).
40. C. Chen, J. Liu, and K. Amine, *J. Power Sources*, **96**, 321 (2001).
41. J. C. Burns et al., *J. Electrochem. Soc.*, **158**, A1417 (2011).
42. R. Petibon et al., *J. Electrochem. Soc.*, **160**, A117 (2013).
43. Y. Itou, N. Ogihara, and S. Kawauchi, *J. Phys. Chem. C*, **124**, 5559 (2020).
44. S. Solchenbach, D. Pritzl, E. J. Y. Kong, J. Landesfeind, and H. A. Gasteiger, *J. Electrochem. Soc.*, **163**, A2265 (2016).
45. S. Solchenbach, X. Huang, D. Pritzl, J. Landesfeind, and H. A. Gasteiger, *J. Electrochem. Soc.*, **168**, 110503 (2021).
46. S. Oswald, M. Bock, and H. A. Gasteiger, *J. Electrochem. Soc.*, **170**, 090505 (2023).
47. R. Morasch, J. Keilhofer, H. A. Gasteiger, and B. Suthar, *J. Electrochem. Soc.*, **168**, 080519 (2021).
48. R. Kötz and M. Carlen, *Electrochim. Acta*, **45**, 2483 (2000).
49. J. Moškon, M. Pivko, R. Dominko, and M. Gaberšček, *ECS Electrochem. Lett.*, **4**, A4 (2014).
50. M. Oldenburger et al., *J. Energy Storage*, **21**, 272 (2019).
51. A. E. Bumberger, C. Steinbach, J. Ring, and J. Fleig, *Chem. Mater.*, **34**, 10548 (2022).
52. A. E. Bumberger et al., *Chem. Mater.*, **35**, 5135 (2023).